

Scientific Basis and Initial Evaluation of the CLAVR-1 Global Clear/Cloud Classification Algorithm  
for the Advanced Very High Resolution Radiometer

Larry L. Stowe, Paul A. Davis<sup>\*</sup>, and E. Paul McClain<sup>\*</sup>

Office of Research and Applications, NOAA/NESDIS, Washington, DC, 20233

Received\_\_\_\_\_; Accepted\_\_\_\_\_

Manuscript resubmitted to *Journal of Atmospheric and Oceanic Technology*.

May 1, 1998

Short Title: Clear/Cloud Classification Algorithm for AVHRR Data

<sup>\*</sup> Private Contractors (Retired from NOAA/NESDIS)

## ABSTRACT

An algorithm for the remote sensing of global cloud cover using multi-spectral radiance measurements from the Advanced Very High Resolution Radiometer (AVHRR) on-board NOAA polar orbiting satellites has been developed. The CLAVR-1 (Clouds from AVHRR-Phase I) algorithm classifies 2x2 pixel arrays from the GAC (Global Area Coverage - 4 km resolution) archived database into CLEAR, MIXED, and CLOUDY categories. The algorithm uses a sequence of multi-spectral contrast, spectral and spatial signature threshold tests to perform the classification. The various tests and the derivation of their thresholds are presented. CLAVR-1 has evolved through experience in applying it to real-time NOAA/11 data, and retrospectively through the NOAA/NASA AVHRR Pathfinder Atmosphere (PATMOS) project, where 16 years of data have been reprocessed into cloud, radiation budget and aerosol climatologies. The classifications are evaluated regionally with image analysis, and it is concluded that the algorithm does well at classifying perfectly clear pixel arrays, except at high latitudes in their winter seasons. It also has difficulties with classifications over some desert and mountainous regions, and when viewing regions of ocean specular reflection. Generally, the CLAVR-1 cloud amounts, when computed using a Statistically Equivalent Spatial Coherence method, agree to within about 5% - 10% of image/analyst estimates, on average.

## 1.0 INTRODUCTION

As numerical weather prediction and climate models become more sophisticated, they demand more accurate observations of atmospheric variables in order to validate the modeling of physical processes, as well as to assign initial values to the cloud parameters (Slingo 1990; Schiffer & Rossow 1983). The lack of accurate cloud physical processes in climate models is currently thought to be the major source of uncertainty in the prediction of climate change due to the "greenhouse" effect (Cess et al. 1989). Therefore, accurate remote sensing of cloud parameters is essential to the improvement of predictive model accuracies, as well as for monitoring climate change.

As an example, if the Earth is about 50% cloud covered, as has been observed from Nimbus-7 (Stowe et al. 1989), and if the seasonally and globally averaged cloud radiative effect is to cool the Earth by about  $25 \text{ W/m}^2$ , (Ardanuy et al. 1989), a one percent change in cloud cover with no change in cloud properties would change the cloud radiative effect by about  $0.5 \text{ W/m}^2$ . As doubling the amount of carbon dioxide gas in the atmosphere would heat the Earth/atmosphere system by about  $4 \text{ W/m}^2$ , this could be compensated by an increase in cloud amount of about 8%, a negative feedback effect of clouds. If cloud amount decreased as a consequence of the doubling of  $\text{CO}_2$ , at this time equally plausible, then the Earth would heat by an additional  $1 \text{ W/m}^2$  for every 2 percent decrease in cloud amount, a positive feedback. Therefore, accuracy in cloud amount is important.

NOAA is developing a cloud remote sensing capability using AVHRR and TOVS (HIRS and MSU) measurements that could satisfy these weather and climate applications (Stowe 1991) because: 1) older cloud remote sensing programs such as ISCCP (International Satellite Cloud Climatology Project, Rossow et al. 1993) or RTNeph (Real-Time Nephanalysis, Hamill et al. 1992) are restricted to only two of the many available channels from the NOAA POES (Polar Orbiting Environmental Satellites) instruments, limiting their ability to detect cirrus and low stratus clouds and to describe cloud properties over certain surface types, such as polar snow and ice, or to account for particle size effects on the retrieved cloud optical properties; and 2) these other programs don't provide for the accurate computation of cloud amount from partially cloud-filled pixels. These limitations can be overcome with multi-spectral approaches based on the physical discrimination features that

separate clouds from background Earth scenes. Examples of these approaches can be found in the literature, but none has been developed for global applications (e.g. Coakley & Bretherton 1982; Saunders & Kriebel 1988; Welch et al. 1988; Baum et al. 1992; Uddstrom & Gray 1996). Additionally, data sets such as ISCCP are retrospective (non real-time) and climatological (sampled data sets averaged over large spatial areas) in design, and cannot therefore meet the demands by the National Weather Service and NOAA/NESDIS for near real-time cloud products with high spatial resolution. Working in real-time, the method described here has the potential of favorably impacting the quality of other climate-related products being produced at NESDIS (e.g., sea surface temperature (McClain et al. 1985), aerosol optical thickness (Stowe et al. 1997), and vegetation index (Tarpley et al. 1984)) by providing cloud screening information for the acquisition of clear-sky pixels. Tests are underway to evaluate the usefulness of CLAVR-1 (Clouds from AVHRR Phase I) as a "front-end" processor and clear/cloud classifier in the generation of NESDIS products.

In this article, the CLAVR-1 global clear/cloud classification algorithm and its evaluation are described more fully than previously (Stowe et al. 1991, Hou et al. 1993, Stowe et al. 1995). It is the initial step in remote sensing of global cloud cover using multi-spectral radiance measurements from the Advanced Very High Resolution Radiometer (AVHRR) on-board NOAA polar orbiting satellites. The objectives of the CLAVR-1 algorithm are operational real-time processing to classify each 2x2 GAC pixel array (adjacent pixels on adjacent scan lines) as CLOUDY, MIXED, or CLEAR; and to map total cloud amount on a global grid. A second generation algorithm, CLAVR-2, has been developed at the pixel level to provide estimates of cloud cover by cloud type and layer. This major modification to the CLAVR-1 algorithm was needed to provide estimates of cloudiness in multiple atmospheric layers, as required by the weather and climate prediction communities (Rossow et al. 1993; Mokhov & Schlesinger 1993 & 1994; Wylie et al. 1994). The Multiple-Layer Cloud Analysis (MLCA) algorithm is described and validated in two papers currently in preparation for submission to this journal (Davis et al. 1998, Luo et al. 1998). A third generation algorithm, CLAVR-3, uses predicted cloud/no-cloud thresholds from an analysis of previously sampled clear-sky radiance statistics (Stowe et al. 1993), to increase the quantity while maintaining the quality of individual CLEAR pixels by reclassifying 2x2 pixel arrays which were considered ambiguous in CLAVR-1. This algorithm is described in a companion paper in this issue (Vemury et al. 1998) which contains additional evaluation tests to further verify the quality of the CLEAR classifications from CLAVR-1 & 3.

The scientific basis of cloud detection with multi-spectral imager data is given in Section 2. Application of these basics to global AVHRR data is discussed in Section 3, and Section 4 describes the cloud test sequencing and treatment of ambiguities. Qualitative and quantitative regional evaluations of the algorithm follow in Section 5; and discussion and concluding remarks comprise Section 6. Comprehensive decision-tree flow charts are presented in the Appendix, together with details of the derivation of some of the tests, their associated thresholds, and other related matters.

## 2.0 BASES OF CLOUD DETECTION WITH MULTI-SPECTRAL IMAGER DATA

Before describing the CLAVR-1 daytime and nighttime cloud classification algorithms in Section 3 and the Appendix, the basis from which the Earth's clouds can be detected with multi-spectral imagery (i.e., contrast, spectral, and spatial signatures) are briefly discussed. A multi-spectral imager provides measurements of the radiance (energy/area/solid angle/spectral interval) for each discrete element of the image (pixel). These radiances can be described with radiative transfer theory. In the solar part of the spectrum (0.3 to 3 micrometers), the incident solar radiation dominates the thermally emitted radiation. The amount reflected depends on the physical and chemical composition of the Earth's surface and atmosphere. This composition is what distinguishes types of Earth surfaces and atmospheric constituents. Differences in composition generally make some components highly reflective (clouds, snow and ice), others moderately reflective (deserts, barren land), and yet others lowly reflective (ocean, vegetation), Davis et al. 1984. This property can be used to detect the presence of some of these components by differences in their reflectance, i.e. "contrast signatures".

Composition differences also cause these components to reflect solar radiation more efficiently in some parts of the spectrum than in others. This latter property can be used as a "spectral signature" to remotely detect the presence of certain surface/atmospheric components. For example, snow reflects very well at wavelengths below about 1 micrometer, and very poorly beyond about 1.5 micrometers, while green vegetation reflects poorly below 0.7 micrometers, but moderately well beyond 0.8 micrometers (Davis et al. 1984; Dozier & Warren 1982). Also, clouds tend to scatter sunlight uniformly with wavelength, whereas haze tends to scatter more at the shorter wavelengths (Nakajima & King 1989; Deirmendjian 1969).

Finally, the varying spatial structure of the Earth/atmosphere composition can be used to differentiate between its different components, i.e., "spatial signatures". For example, the ocean has a very uniform reflectance over hundreds of kilometers, whereas some clouds, mountainous terrain, and sparse vegetation have highly variable reflectances over tens of meters (e.g., Wielicki & Parker 1992).

In the thermal infrared, from about 3 to 20 micrometers, Earth/atmosphere components may also be discriminated by these three types of signatures, but they result from a different physical process, absorption and re-emission of radiation, rather than from reflection and scattering. Infrared radiation is proportional to scene temperature, and thus contrast signatures are those that separate cold from hot surfaces, e.g., clouds over deserts in daytime. Spectral signatures are those where the emissivity of surfaces vary with wavelength, such as between thin cirrus clouds and atmospheric water vapor in the 10 to 12 micrometer region of the spectrum (King et al. 1992). Finally, spatial signatures exist due to differences in scale between spatial inhomogeneities in the clouds and the underlying surface (Coakley & Bretherton 1982).

Cloud retrieval algorithms also generally separate themselves into daytime (solar reflectance and infrared emittance) and nighttime (infrared emittance only) algorithms. Because of the inherent differences in the two principal Earth surfaces, they also separate themselves by land and ocean. Each of these will be explored further in Section 3, where a clear/cloud classification algorithm is developed for global applications with NOAA/AVHRR data, i.e., the CLAVR-1 algorithm.

### 3.0 APPLICATION OF CLOUD DETECTION SIGNATURES TO GLOBAL AVHRR DATA

Clear/cloud remote sensing techniques employing the AVHRR are based on the following five spectral radiance-measuring channels: Ch 1 (centered at 0.63  $\mu\text{m}$ ) measures reflected visible radiation, which is weakly attenuated by ozone absorption and by molecular and particulate scattering. Ch 2 (centered at 0.83  $\mu\text{m}$ ) detects reflected near-infrared (NIR) radiation, which is moderately attenuated by water vapor, but less affected by molecular and particulate scattering. Chs 3, 4 and 5 (centered at 3.7, 10.8, and 11.9  $\mu\text{m}$ , resp.) detect emitted radiation in the thermal-IR, where attenuation is primarily by water vapor, increasing in strength as wavelength

increases. Ch 3 is also sensitive to solar radiation reflected by the Earth's surface and clouds, and it is only weakly attenuated by particulate scattering (Deirmendjian 1969).

The philosophy of applying these principles to AVHRR global data for operational real-time and retrospective derivation of climate-quality cloud products is based on the following requirements: 1) minimize auxiliary data to aid the classifications, thus reducing dependence of derived quantities on other independently measured climate variables, such as surface temperature; 2) avoid multiple passes through the data, which could provide AVHRR-specific information to aid in threshold setting, but increase processing time; and 3) base the algorithm on already proven operational real-time AVHRR cloud detection algorithms to increase the likelihood of success while minimizing development efforts.

This approach has led to the development of a multi-spectral, sequential, decision-tree threshold algorithm---CLAVR-1. The test thresholds do not vary with Earth location or season (universal), although some depend on infrared brightness (equivalent blackbody) temperature.

Past and current operational approaches at NOAA/NESDIS use cloud detection algorithms that are application-specific, e.g. the MCSST, (McClain et al. 1985) in that they discard information about the clouds themselves. CLAVR adopts a more "generic" approach, i.e. one that works for all applications, and one that detects clear and cloudy satellite observations over both land and sea, day and night, and even over snow, ice, and deserts.

Details of the CLAVR-1 daytime and nighttime cloud classification algorithms are described in the Appendix, including comprehensive decision-tree flow charts. In the present section the various cloud tests are grouped according to the type of "signature" test employed (see Section 2). Discussion of the cloud test sequencing and thresholding, and tests for ambiguities, are also found in this section. Some threshold-setting details are discussed in the Appendix.

### 3.1 Contrast Signature Tests

Thresholds are required in the application of contrast signature tests. The assignment depends on the Earth

surface type, cloud type, and whether the channel measures reflectance or emittance. The contrast signature tests all have the same characteristic: a pixel value is compared against a threshold value that is intended to separate cloudy pixels from all others. These thresholds can be determined either theoretically, empirically or from past experience. Here it was chosen to set them empirically and from past experience, as it is very difficult to simulate all possible cloud/surface observation conditions with theoretical models.

### Reflectance Tests

Some of the daytime tests use observed bidirectional reflectances. These reflectance factors (referred to as albedo) are derived from the observed signal for each pixel stored in the NOAA Level 1b data sets using formulae and coefficients from Kidwell (1991). These reflectance factors are converted to equivalent-isotropic albedos by dividing by the cosine of the solar zenith angle, and multiplying by the square of ratio of Earth-Sun distance at time of observation to the mean Earth-Sun distance. They are further adjusted for calibration drift with time by the formulae of Rao & Chen (1994).

Two reflectance-based cloud tests have been developed for CLAVR-1. One utilizes the reflectance in Ch 1 over land or in Ch 2 over ocean, and is referred to as the Reflectance Gross Cloud Test (RGCT). Another is the Ch 3 Albedo Test (C3AT). A useful value for the Ch 2 reflectance (R2) threshold for the RGCT over the ocean is 30%. Empirical studies have shown that this is a representative value for the albedo of homogeneous low-cloud fields and that it is not usually exceeded by specular reflection from the ocean. It also matches the cloud filtering threshold used in processing for the NOAA/AVHRR aerosol optical thickness product (McClain 1989).

Over land the RGCT uses Ch 1 reflectances (R1) instead of Ch 2 because Ch 2 is more sensitive to vegetation and is thus more highly reflective and variable, tending to minimize the contrast signature. A threshold of 44% has been found empirically to work well in detecting cloud over land. Gutman et al., 1995, confirm this RGCT threshold except for small areas in the Saharan desert in winter, where it can be exceeded. However, daytime temperature in desert areas is usually higher than expected for cloud, so such ambiguities can be removed. (See Sec. 4.3 for description of restoral tests used to remove such ambiguities).

The C3AT is introduced to detect weakly-reflecting clouds (some cirrus, or water clouds that are thin or sub-pixel in size). This test is also very useful in separating the effects of these weakly scattering clouds from atmospheric haze. This is because the larger cloud particles scatter sunlight more effectively than aerosol



particles at 3.7 micrometers (Deirmendjian 1969). This test is used in a somewhat modified form in the operational aerosol retrieval program at NESDIS (McClain 1989). As the Ch 3 radiance in daytime is a combination of emitted and reflected radiation, it is necessary to strip out the emitted portion using an estimate of it derived from Chs 4 and 5. What remains is an estimate of the reflected radiance, which is converted into a Ch 3 equivalent-isotropic albedo (see Eqn A2 in Appendix). Cloudfree land surfaces are appreciably brighter than the ocean. Accordingly, empirical C3AT thresholds have been found to be about twice the value used over the sea.

### Emittance Tests

One emittance-based contrast signature test is used in CLAVR-1, the Thermal Gross Cloud Test (TGCT). Over the ocean the TGCT threshold is based on a limiting minimum infrared temperature for the ocean surface, viz., the freezing point of sea water. It will classify pixels as CLOUDY when the pixel's Ch 4 temperature,  $T_4$ , is below that of freezing sea water. Over land the TGCT threshold is lower than over the sea to prevent the potentially much colder land surfaces from being called CLOUDY. At latitudes where sea ice or snow are likely, contrast and spectral signature tests can be used to remove this ambiguity (see Sec. 4.3 discussion of restoral tests). The value chosen for the TGCT threshold over land is 249K. It is the minimum zonally-averaged, cloudfree, land temperature observed equatorward of 60 deg latitude in daytime in the Nimbus-7 cloud climatology (Stowe et al. 1989).

## 3.2 Spectral Signature Tests

Spectral signature tests involve the difference or ratio of the emittances or reflectances measured in two AVHRR channels. The two emittance channels (Ch 4 & Ch 5) and the combined emittance-reflectance channel (Ch 3) have differing transparencies with respect to upwelling infrared radiation, principally because of water vapor in the atmosphere. The reflectance channels are more useful for resolving ambiguities (see Sec. 4.3).

### Reflectance Tests

The ratio of Ch 2 to Ch 1 reflectances ( $R2/R1$ ), according to Saunders & Kriebel (1988), is  $< 0.75$  for a cloudfree ocean and is between 0.9 and 1.1 for cloud. The latter range is used for the RRCT (Reflectance Ratio

Cloud Test) threshold. Over vegetated land surfaces, this ratio is typically greater than 1.2 (Gutman et al. 1995 show  $\text{NDVI} > 0.1$  for these surfaces, which is equivalent to  $R2/R1 > 1.2$ ), so the same threshold range for cloud detection works for these surface types as well. However, supporting empirical studies have shown that some desert surfaces have  $R2/R1$  ratios in the cloud range, so the RRCT cannot be relied upon over such areas.

### Emittance Tests

One emittance-type cloud/no cloud threshold test is the Ch4-Ch5 (Four-Minus-Five Test - FMFT) brightness temperature difference. It is employed primarily to detect thin cirrus clouds (Inoue 1986; Prabhakara et al. 1988), which can produce larger FMFT values than possible from water vapor attenuation alone. This results from ice particles having a lower emissivity (higher transmissivity) at 10.8 micrometers than at 11.9, creating an FMFT signature similar to that of water vapor. Depending on the thickness of the cirrus, this difference can exceed that due to water vapor alone. The Four-minus-Five Test (FMFT) can also be used to detect cold, water droplet clouds in mid-latitudes (Luo et al. 1995) and in polar latitudes (Yamanouchi & Kawaguchi 1989), as will be explained in the discussion of restoral tests in Sec. 4.3.

The threshold for the FMFT must be chosen to unequivocally indicate the presence of cloud. This threshold is defined to be the maximum FMFT value that is attributable to water vapor alone. We have used the  $T_4$ - $T_5$  temperature-difference dependence on  $T_4$  as an index of atmospheric humidity (cf. McClain et al. 1985; Saunders & Kriebel 1988). As we do not currently have a reliable method of extracting atmospheric water vapor from Earth satellite data, we have generated a simulation database of calculated  $T_3$ ,  $T_4$ , and  $T_5$  brightness temperatures (accounting for each channel's spectral response function) from a large number of globally distributed cloudfree atmospheric soundings over ocean and land using radiative transfer theory. These results are plotted in a scatter diagram in Fig. 1, where the FMFT threshold for ocean is shown. It is essentially the same over land, but it extends to higher values beyond  $T_4 > 295\text{K}$ . As  $T_4$  increases, the maximum value of  $T_4$ - $T_5$  also increases because warmer atmospheres can contain more water vapor. FMFT thresholds were defined by fitting fourth or fifth degree polynomials in  $T_4$  to the maximum values of FMFT for these cloudfree conditions. The details can be found in Sec. A4 of the Appendix.

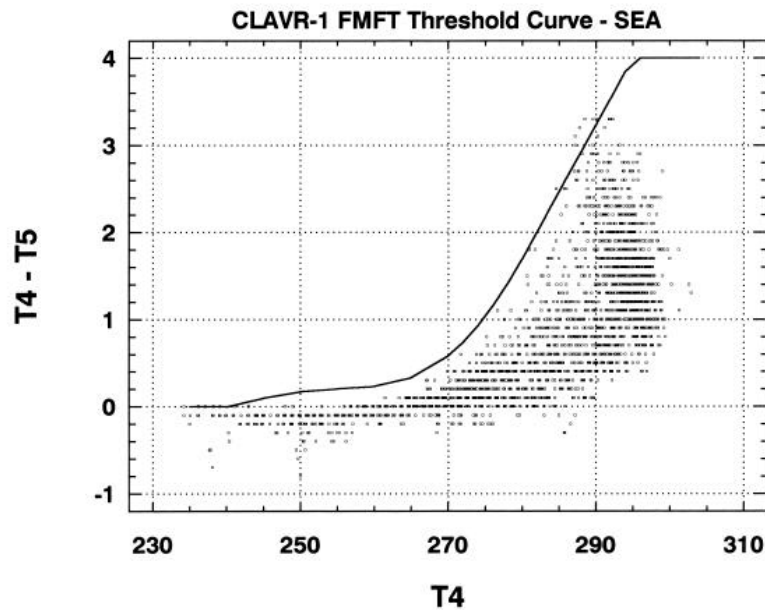


Figure 1. Scattergram of Ch 4 minus Ch 5 (FMFT) brightness temperature difference versus Ch 4 brightness temperature computed from raobs using a radiative transfer model to simulate AVHRR data (cloudfree ocean and cloudfree land combined).

The radiative properties of cloudy and clear atmospheres at 3.7  $\mu\text{m}$  differ from those at 10.8 or 11.9  $\mu\text{m}$ ; viz., clouds are more reflective and the atmosphere is more transparent at 3.7  $\mu\text{m}$  (Hunt 1973), particularly in the case of low stratus clouds, which typically have very small droplet sizes. Based on prior success in cloud-filtering for sea surface temperature estimates (McClain et al. 1985), a Uniform Low Stratus Test (ULST) based on Ch 3 minus Ch 5 temperature differences has proven a powerful

nighttime test because the presence of cloud depresses  $T_3 - T_5$  to substantially negative values (see Fig. A5 in Appendix). The ULST requires a  $T_4$ -dependent threshold to allow for variable water vapor attenuation between the two channels. Using the same cloudfree simulation dataset, the ULST threshold curve, determined from a least-squares fit through a subset taken from the ocean cases, is plotted in Fig. 2. The effect of water vapor absorption is again evident as an exponential increase in this temperature difference with increasing  $T_4$ . The figure is limited to  $T_4 > 271\text{K}$  because it has been used extensively only over cloudfree and ice-free oceans. Its polynomial representation and other details can be found in Sec. A4 of the Appendix.

The relatively high optical transmittance of most cirrus clouds at 3.7 micrometers (Hunt 1973) combines with the increased dependence of the Planck blackbody-radiance on temperature at this wavelength to yield large  $T_3 - T_5$  differences for cirrus clouds. These temperature differences are the basis for a nighttime Cirrus Test (CIRT), which uses the function  $(T_3 - T_5)/T_5$ . Again, the cloudfree simulation data base was used to define a  $T_4$ -dependent threshold for the CIRT to account for water vapor variations. These results are plotted in Fig. 3, again showing

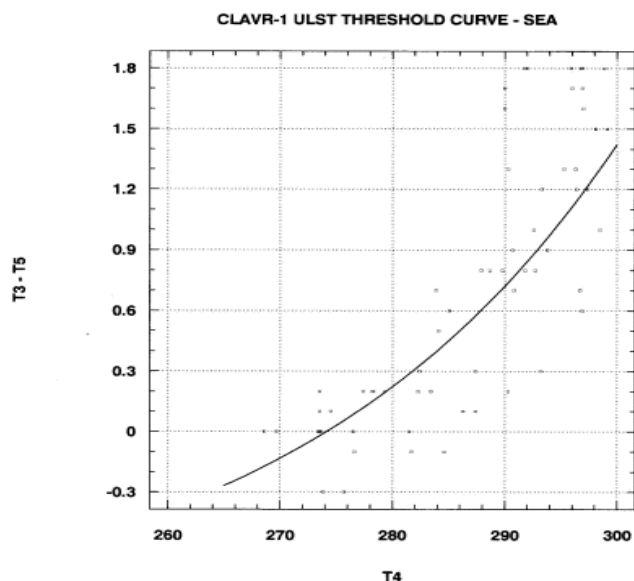


Figure 2. Scattergram of Ch 3 minus Ch 5 (ULST) brightness temperature difference versus Ch 4 brightness temperature ( $T_4 > 271K$ ) computed from raobs using a radiative transfer model to simulate AVHRR data for a cloudfree ocean at night.

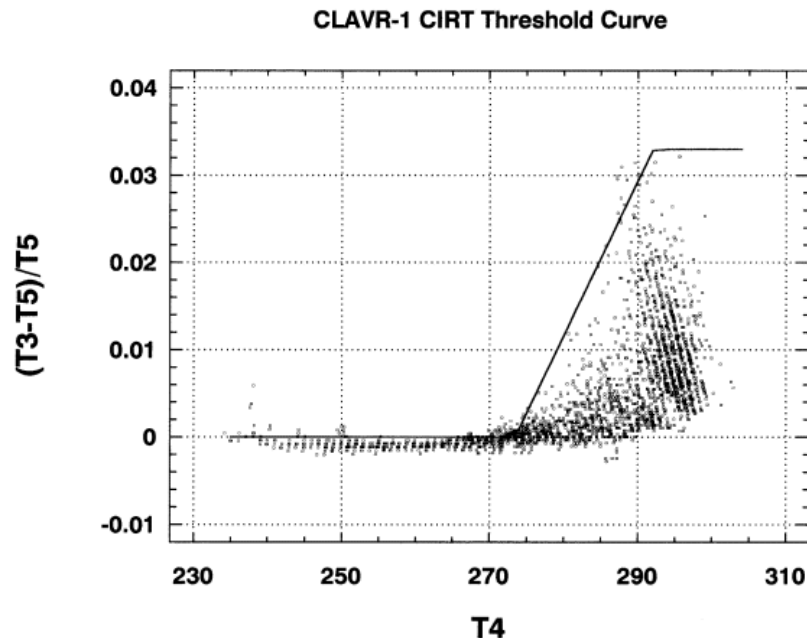


Figure 3. Same as Figure 1 & 2 except that  $(T_3 - T_5)/T_5$  (CIRT) is plotted versus  $T_4$ . CLAVR-1 CIRT threshold curve superimposed on data.

an increase in temperature difference with  $T_4$ . Analysis of the upper envelope of this relationship led to the threshold curve that is discussed in Sec. A4 of the Appendix.

### 3.3 Spatial Signature Tests

Spatial signature tests depend on the observation that, on the scale of  $2 \times 2$  pixel arrays, the scene viewed by the AVHRR is relatively more "uniform" in the absence of clouds than with clouds (McClain, et al, 1985), and this is true whether reflectance (daytime) or emittance (daytime or nighttime) is used.

#### Reflectance Tests

It has been found that reflectance variability  $> 0.3\%$  rarely occurs over cloudfree oceans in the absence of sun glint, so this is used for a Reflectance Uniformity Test (RUT) threshold (McClain et al. 1985). Glint areas, however, are generally quite uniform thermally in the absence of clouds, so they are handled by a special "restoral" test (discussed in Sec. 4.3). Cloudfree land surfaces are naturally more variable in reflectance than ocean surfaces, therefore the RUT land thresholds must be greater

than over the ocean. A value of 9% was derived empirically from image analysis studies. Mountainous regions may have spatial variability greater than this threshold and, without ancillary information, may be called cloud contaminated erroneously. As is the case with the RGCT (see Sec. 3.1), Ch 2 reflectances are used for the RUT over ocean and Ch 1 reflectances over land.

#### Emittance Tests

Experience has shown that when the ocean is cloudfree it is almost always quite spatially uniform in the infrared. The Thermal Uniformity Test (TUT) threshold, separating cloudfree from cloud contaminated, has been found empirically to be 0.5K over the oceans. This is slightly greater by 0.2K than the threshold used in the operational MCSST algorithms (McClain et al. 1985). Over land, the maximum variability of Ch 4 temperature ( $T_4$ ) characteristic of cloudfree scenes has been found empirically to be six times larger than over the ocean because of the far less homogeneous thermal conditions and variable emissivities over land surfaces.

### 4.0 Cloud Test Sequencing for Clear/Cloud Classifications - The CLAVR Phase I Algorithm

The various contrast, spectral, and spatial cloud signature tests described in the foregoing sections have been assembled into a sequential, decision-tree, multi-spectral threshold algorithm. This algorithm uses space/time-invariant {i.e., universal} thresholds either derived theoretically, empirical or from past experience to identify CLEAR, MIXED, and CLOUDY 2x2 GAC pixel arrays. The algorithm sequence and thresholds have been optimized for four scene conditions: day/land, day/ocean, night/land, and night/ocean. The overall philosophy of the test sequences is to classify the clouds within each pixel array, first by their gross signatures and subsequently by their more subtle ones. This provides an algorithm that is efficient in computer time, and it ensures that pixels failing all the tests in the sequence have a very small probability of radiatively-significant cloud cover in them. The precise choice of which cloud test should be first, second, etc. was first based on physical/meteorological reasoning. The sequencing was occasionally adjusted later based on experience with the algorithm and by analyzing test cases. Much prior experience with the MCSST algorithms was invaluable in this process. Ambiguities in classification are handled by what are called "RESTORED-CLEAR" tests. Specifics of the algorithm are described in the next three subsections, with more detail provided in the Appendix.

#### 4.1 Daytime

The daytime (solar zenith angle  $< 84.3$  deg) ocean and land cloud-test sequence, the display color used in Sec. 4 to identify each test in an image, the AVHRR channels, and the test thresholds (with footnotes identifying how they were derived) are listed in Table 1. Also listed are the CLEAR restoral tests and the colors used to describe the pixels classified as CLEAR. Also, two columns give the frequency of occurrence of this sequence of tests for a one day (format: CLOUDY classification/MIXED classification). A flow chart description of the algorithm is found in the Appendix, Figs. A1 (ocean) & A2 (land).

In general, a 2x2 pixel array is classified CLEAR only if all four pixels fail all the cloud tests listed. If any of the pixels pass any of these tests, the array is considered cloud contaminated. However, RESTORED-CLEAR tests (see Sec. 4.3) are applied to indicate "possibly CLEAR" (i.e., if the pixel could be cloudfree snow/ice, desert, or ocean viewed in the specular direction). If all four pixels in the array pass a cloud test and are not restored to CLEAR, the array is called CLOUDY. If only one to three pixels follow this path, the pixel array is called MIXED. This classification implies a mixture of cloudy and cloud-free pixels, or fully cloudy pixels with variable cloud heights/thicknesses, or partly cloudy pixels with varying cloud properties within the 2x2 array. For the same reasons, a pixel array that passes a spatial signature test (uniformity) is also classified MIXED. As is evident in the distribution of cloud test occurrences in Table 1, the most powerful cloud tests are the contrast and spatial signature tests, with the spectral signature tests assisting with detection of cloud types weakly affecting the radiation field (e.g. thin cirrus).

A better sense of the algorithm can be obtained from the flow charts (Figs. A1 & A2) presented in the Appendix. Except for threshold values, the ocean and land daytime algorithms are essentially the same. The Reflectance Gross Cloud Test (RGCT) detects thick clouds and the Reflectance Uniformity Test (RUT) detects thinner, horizontally non-uniform cloud. The Reflectance Ratio Cloud Test (RRCT) and the Ch 3 Albedo Test (C3AT) detect thinner, horizontally-uniform clouds, identifying clouds missed by the previous tests. The latter is particularly good at separating cloud from haze. The RRCT and C3AT are bypassed over deserts because they cannot unambiguously detect clouds over these surfaces. Also, the C3AT is skipped when within the cone of specular reflection (see Sec. 4.3). Three thermal tests follow these reflectance tests to detect clouds too optically thin to be classified as cloud by them. In sequential order, the Thermal Uniformity Test (TUT), detects non-uniform cloud; The Four-Minus-Five Test (FMFT) detects optically thin cirrus; and the last, the Thermal Gross Cloud Test (TGCT), detects thicker cloud (the latter test is excluded near the poles). The cloud tests that use Ch 3, 4, or 5 temperatures are suspended when the Ch 4 temperature exceeds 315K because these channels saturate and cannot be used reliably in such conditions. The day and night CLEAR restoral logic is described in Sec. 4.3.

## 4.2 Nighttime

Cloud test sequencing at night is again the same for ocean and land, only the thresholds and treatment of desert surfaces are different. It is also much simpler than the daytime sequencing. There are only emittance tests. The test sequence for land and ocean is given in Table 2, which contains information like that in Table 1. At night, the sequence begins with the Thermal Gross Cloud Test (TGCT), which detects thick cold clouds. This is followed by the Thermal Uniformity Test (TUT), which serves the same function as it did in daytime, to detect non-uniform cloud not cold enough to be detected by the prior TGCT. As in the daytime, the contrast and spatial signature tests account for between about 60% (land) and 80% (ocean) of the classifications. The next test in the sequence is the Uniform Low Stratus Test (ULST), which is able to detect low altitude, water-droplet clouds, primarily over oceans, as is seen by the frequencies in Table 2. Because of reduced emissivity of deserts at 3.7 micrometers, and also because of poor Ch 3 precision at very low temperatures, this test is suspended over deserts or when temperatures fall outside the range 271K to 289K over land (see Eqn A4, Appendix). The Four-Minus-Five Test serves the same purpose as it does in daytime, detection of thin cirrus. As in the daytime, it is much more effective at doing this over land, partly because the land sequence allows more pixels to be tested.

The final test is the Cirrus Test (CIRT), which uses the Ch 3 - Ch 5 brightness temperature differences to detect thin cirrus. This test is bypassed if the Ch 1 digital count value is greater than 45 (its dark scene value is typically about 40 counts) because this indicates the presence of stray light contaminating the AVHRR data. This is prone to occur late in the lifetime of each satellite, and the stray energy erroneously elevates the Ch 3 temperatures, giving false thin cirrus cloud classifications.

The nighttime decision trees are also simpler than the daytime ones in that they have only one restoral test (described in Sec. 4.3). As in the daytime algorithms, the classification of 2x2 arrays as CLEAR, MIXED, or CLOUDY depends on testing the four pixels in each array. More detail is given in the Appendix, where flow charts of the nighttime algorithms are presented as Figs. A3 (ocean) & A4 (land), to help illustrate the process.

#### 4.3 Treatment of Ambiguous Classifications (Restorals to CLEAR)

There are situations in which a given cloud test can be passed erroneously, e.g. when snow, ice, or sun glint yields a Ch 1 or 2 reflectance that exceeds the RGCT threshold. When this happens, it is sometimes possible to "restore" the pixel array to a path on the decision tree (see flow charts in Figs. A1-A4 of the Appendix) that could eventually lead to a CLEAR snow/ice, land or ocean classification (provided no subsequent "restored cloud" tests are passed). For this to happen, all four pixels of the 2x2 array must pass the restoral test. Although the typical frequency of occurrence of RESTORED-CLEAR classifications, as indicated in Table 1, is quite small, they can be important in getting an accurate portrayal of cloudfree conditions. The next two subsections briefly describe the various restoral tests used in CLAVR-1, and details for daytime are covered in Sec. A6 of the Appendix.

##### Daytime Restoral Tests

When a 2x2 array is highly reflective in Ch 1 or Ch 2 and relatively dark in Ch 3, it is considered likely to be a CLEAR array situated over snow or ice. Consequently, applying a Ch 3 Albedo Test provides a mechanism for restoring these potentially-CLEAR pixels to a RESTORED-CLEAR classification after they have erroneously passed either the RGCT, the RUT, or the RRCT cloud tests (see Figs. A1 and A2 of the Appendix).



Deserts and other arid land types can have surface albedo conditions that satisfy any of the four reflectance-based cloud tests. If these land types are actually cloudfree, however, they usually have brightness temperatures that exceed those associated with clouds, at least for the afternoon satellites (NOAA-7, 9, 11, & 14). Thus, to remove this ambiguity, all pixels passing these tests are subjected to a Thermal Gross Cloud Restoral (TGCR) test. Any MIXED or CLOUDY array where all four pixels have  $T_4$  greater than the TGCR threshold are classified as RESTORED-CLEAR. Because some non-desert land surfaces exhibit Ch 3 albedos greater than the C3AT threshold, pixels passing the C3AT are also subjected to a Thermal Uniformity Restoral (TUR) test before the TGCR is invoked. If the 2x2 pixel array is sufficiently uniform thermally, it is classified RESTORED-CLEAR and a specific cloud code is assigned to indicate this path.

In an attempt to remove the sunglint-related ambiguity that can be present in all four reflectance tests over the ocean, a TUR test (in this case using a limit of  $<0.5K$ ) is applied when the satellite is viewing within the expected region of specular reflection (see Sec. A5 of the Appendix).

To increase the probability that RESTORED-CLEAR pixel arrays are CLEAR, they are subjected to several infrared cloud tests. First a TUT is applied (with the threshold set to 3K) over ocean as well as land, as sea-ice is likely to be as non-uniform as land. They are also subjected to an FMFT and, over non-polar land, a TGCT. The former looks for thin cirrus and the latter for deep glaciated clouds, both of which may exhibit low Ch 3 albedos because of their ice content. If any of these tests is passed, the pixel array is considered MIXED or CLOUDY (if all four pixels pass the test) and the cloud codes are modified to indicate the decision-tree path followed (see flow charts, Figs. A1 & A2, in the Appendix).

### Nighttime Restoral Tests

The nighttime algorithm has provision for only one type of RESTORED-CLEAR classification, viz. one allowing for erroneous passing of the Thermal Gross Cloud Test (TGCT). The use of a constant threshold for the TGCT has the potential for mis-classification of pixels at high latitudes where cloudfree, usually snow- or ice-covered surfaces, can reach temperatures low enough to be classified CLOUDY. As shown by Yamanouchi &

Kawaguci (1989), low water clouds over ice- and snow-covered surfaces can be detected by positive Ch4 - Ch5 temperature differences (viz., check if brightness temperature difference between channels 4 and 5 is greater than a channel 4 temperature dependent FMFT threshold). Therefore, all TGCT CLOUDY pixels poleward of 30 degrees latitude, ocean or land, are subjected to a Four-Minus-Five Restoral (FMFR) test. If this test is passed by all four pixels, the pixel array is restored to CLEAR and passes on to the TUT and subsequent cloud tests in the sequence.

## 5.0 INITIAL EVALUATIONS OF THE ALGORITHM

This section shows examples of the performance of the CLAVR-1 algorithm, first on a qualitative, test by test basis; secondly on a quantitative basis where CLAVR-1 values of cloud amount are correlated with an independent estimate in fixed geographical areas by an interactive image processor. Evaluation on a global basis by statistical comparisons with other published satellite cloud climatologies have been published (Hou, et al., 1993) and will also be the subject of future publications.

### 5.1 Qualitative Evaluations of Cloud Tests

Cloud tests from the CLAVR-1 decision-tree sequences were evaluated using five daytime and eleven nighttime GAC scenes. Some were over land and others over the ocean; and some were in winter and others in summer. Geographically they varied from Somalia and Saudi Arabia to the western USA and adjacent waters, and from eastern Siberia to Antarctica. Lack of space permits detailed discussion of only a few of these scenes, but the analyses of all are summarized later in this section. They all show that the CLAVR-1 tests are performing their function of separating clear from cloudy pixels over most times and locations on the Earth.

### 5.1.1 Somalia Area

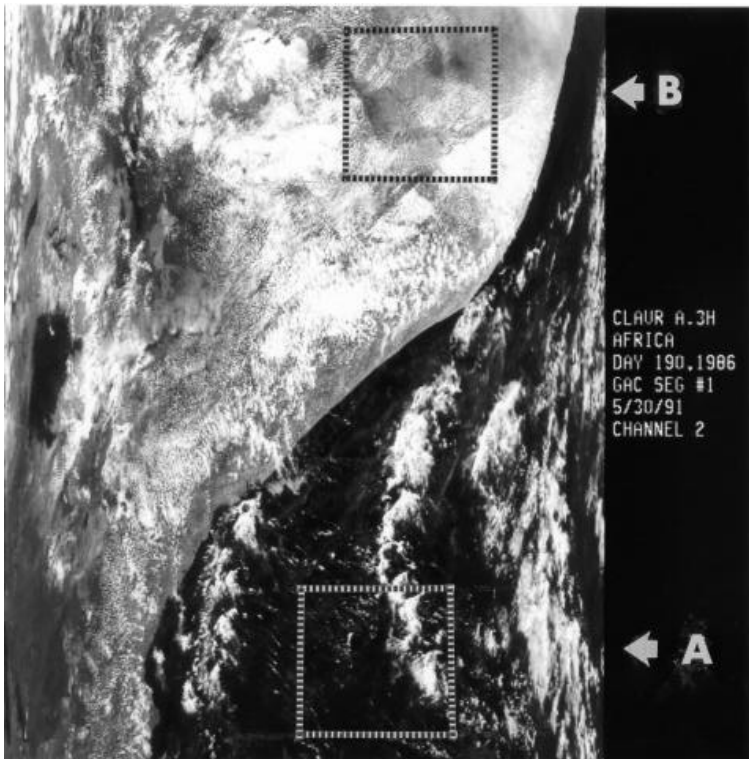


**Figure 4a.** Gray-scale cloud image of an orbital segment of AVHRR Ch 2 GAC reflectance data over eastern tropical Africa in daytime. The location of two test scenes is shown.

Photo-interpretation of . 4a, a standard B/W image of Ch 2 reflectance over the coastline of eastern tropical Africa on July 9, 1986, indicates that, over the ocean, there are mainly scattered, small-scale, clouds characteristic of weak convection. There is some tendency toward meso-scale organization, yielding somewhat stronger convective patterns with elements that are more reflective. The associated Ch 4 thermal-IR image (not shown) indicates, however, that the brighter and more organized cloud masses are little if any deeper (i.e. colder) than the more scattered ones.

Fig. 4b, the same image rendered in color to depict the CLAVR-1 cloud classifications (see Table 1, which shows the color used to depict each cloud test), reveals that the better-organized CLOUDY areas over the ocean are detected by the first

daytime reflectance test (RGCT), the remainder being classified either as CLEAR (black) or MIXED due to non-uniformity of reflectance (RUT). Fig. 4c depicts the distribution of MIXED and CLOUDY pixel arrays, which are subsequently used in the estimation of cloud cover (cf. Sec. 4.2 & 4.3), where a gray shade has been assigned to the MIXED class and a white shade to the CLOUDY class.

Figures 4b & c indicate which test detected the presence of cloud and whether that array was considered MIXED or CLOUDY. In a careful study of the clouds in Scene "A" of Figure 4a, the preponderance of 2x2 pixel arrays were classed as MIXED, with only 8% called CLOUDY and 9% CLEAR. All the CLOUDY ones passed the first test, the RGCT, so the other CLAVR-1 tests were never applied.

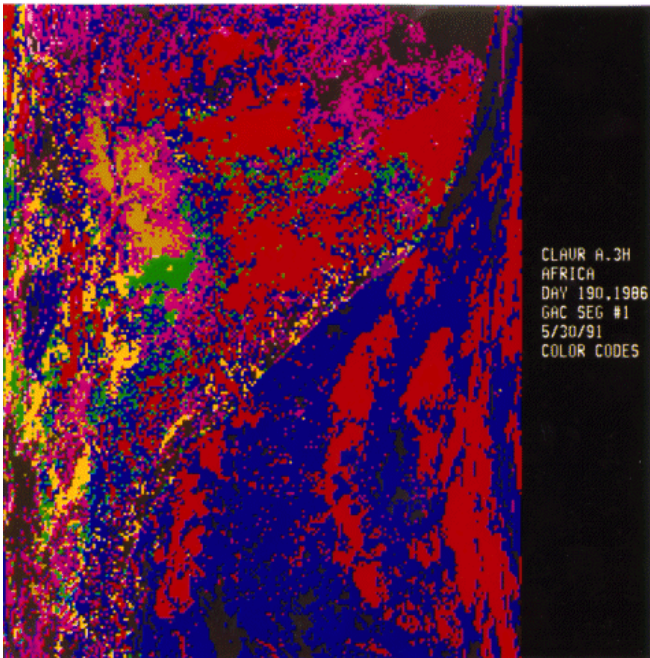


Figure 4b. Color-coded image of the same segment derived from the CLAVR-1 algorithm. Refer to Table 1 and Figures A1&2 to relate color to clear/cloud classification and algorithm path.

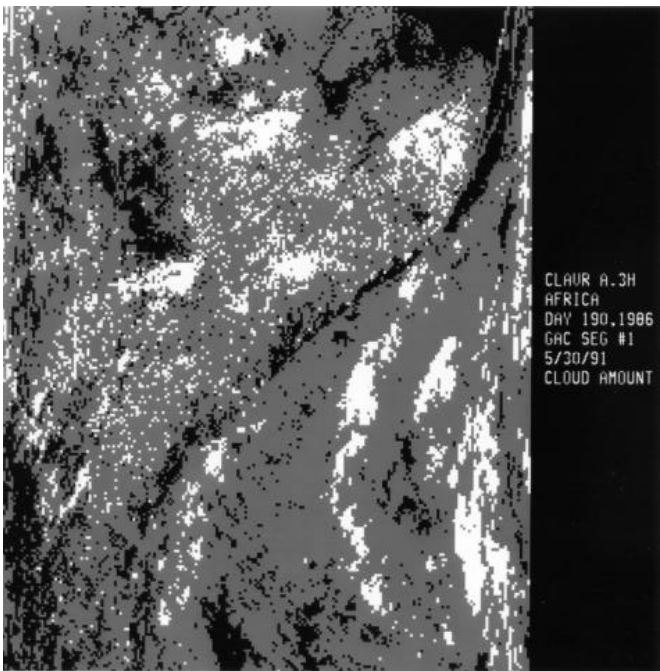
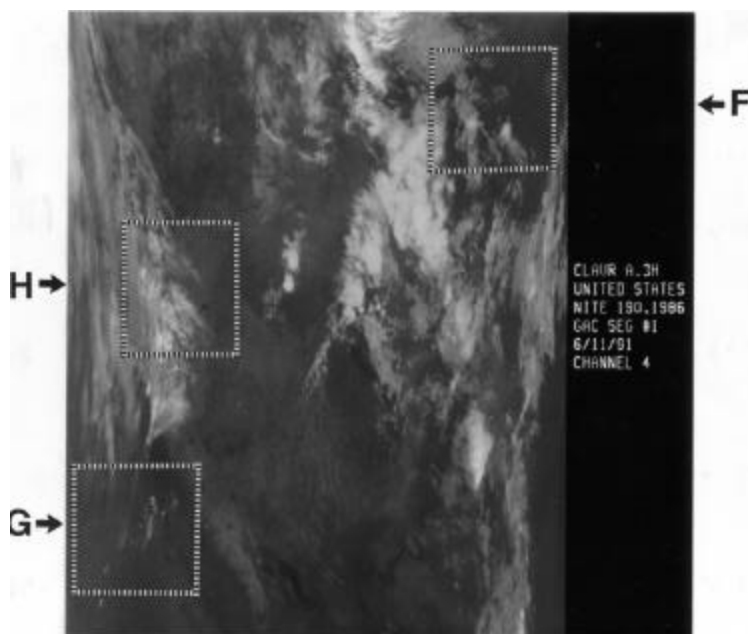


Figure 4c. CLAVR-1 classification of the same segment into three categories of cloud cover: CLOUDY (white); MIXED (gray), and CLEAR (black).

Photo-interpretation of land scene "B" in Figure 4a, shows more widespread cloudiness than was the case over the sea, although again there appears to be no well organized synoptic-scale or deep convective cloud systems present. The MIXED cloud amount category predominates as seen in Fig. 4c, although perhaps not as much as over the ocean. Some differences in cloud type do show up between land and sea in Fig. 4b, however. Because the threshold for the first reflectance test is higher over land, some CLOUDY/MIXED pixels passed other tests (RRCT, C3AT, and TUT). Likewise, some pixels classed as CLEAR resulted from the thermal restoral process (TGCR). In scene "B", the majority of the pixel arrays (68%) were classified as MIXED, although almost 14% were called CLOUDY and about 17% were CLEAR or RESTORED-CLEAR (about 1%). CLAVR-1 classified the CLOUDY arrays mostly on the basis of the RGCT, but a significant number were from the RRCT.

### 5.1.2 Southwestern USA

Three nighttime scenes in the southwestern USA ("F", "G", and "H") are depicted in Figure 5a. They are part of a Ch4 (10.8  $\mu\text{m}$ ) brightness temperature GAC image (low temperatures are white) from a descending segment of an orbit on July 9, 1986. Scene "F" is entirely over land in the high plateau area, whereas "G" is mostly over the ocean just off the California coast. Scene "H" is farther north along the coast, but virtually completely over land. Figs. 5b and



**Figure 5a.** Gray-scale cloud image of an orbital segment of AVHRR Ch 4 GAC temperature data over the southwestern USA in nighttime. The location of three test scenes is shown.

5c are of the same type as Figs. 4b and 4c.

Photo-interpretation of the ocean portion of Fig. 5a is made difficult by a lack of thermal contrast between any low-level clouds present and the underlying ocean surface. The coldest clouds are well inland and appear as several organized clusters or bands, some portions of which are convective in appearance. There is a fairly substantial amount of cloudfree land area, which is classed as CLEAR by the CLAVR-1 algorithm (see Figs. 5b and 5c). The scattered distribution of MIXED arrays in this image, most noticeable in Fig. 5c, is probably the result of terrain-induced effects vis a vis the Ch 4

temperature uniformity test (TUT). The deeper and more organized convective clusters over land, as well as a more stratified-appearing cloudy area near the coast (middle and upper left edge of Fig. 5b), are easily detected from their low temperatures (TGCT). Most noteworthy, however, is that low-level stratus over the ocean has been detected by the ULST spectral-signature test (lower left edge of Fig. 5b). The presence of this type of cloud in this area is consistent with surface-based climatology (Warren et al., 1988). Other low stratus (yellow) patches are seen over land in Fig. 5b, the largest being found in the upper right corner in Area F. One other CLAVR-1 cloud type, thin cirrus (FMFT), is found in this segment in significant amounts, but over rather limited areas.



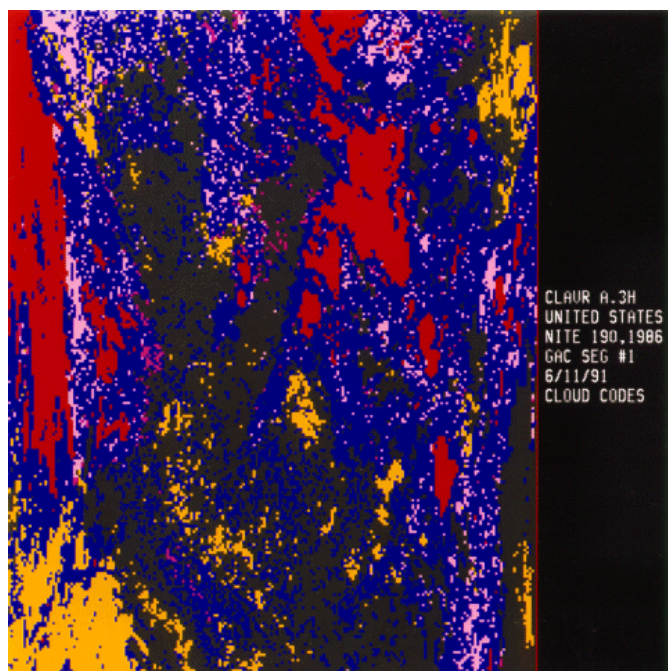


Figure 5b. Same segment shown in Fig. 5a, but showing color-coded classifications derived from the CLAVR-1 algorithm. Refer to Table 2 and Figures A3&4 to relate color to clear/cloud classification and algorithm path.

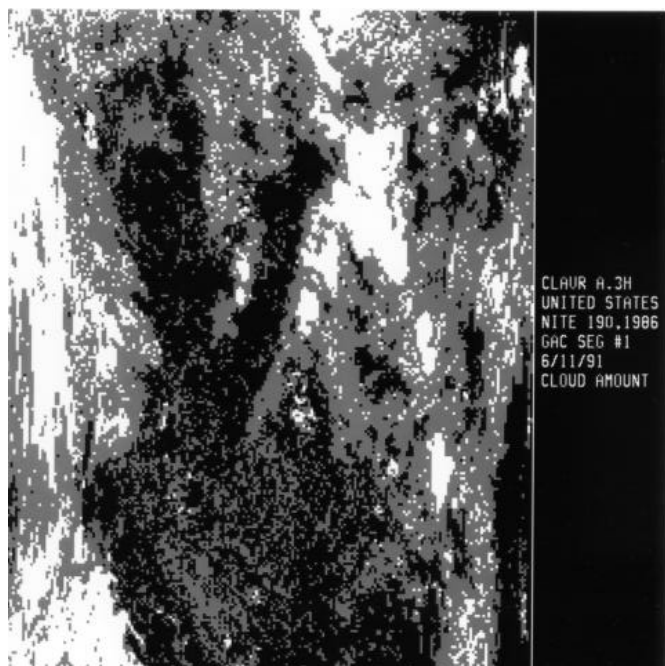


Figure 5c. CLAVR-1 classification of the same segment into three categories of cloud cover: CLOUDY (white); MIXED (gray), and CLEAR (black).

A statistical analysis shows that CLAVR-1 classified Scene "F" as predominantly MIXED (55%) or CLEAR (34%), with the CLOUDY (11%) areas being predominantly made up of low stratus (58%) or thin cirrus (25%). The MIXED pixel arrays result predominantly from the TUT (76%). The thin cirrus arrays (FMFT) are mostly associated with a layer of clouds colder than the low stratus arrays. The low stratus classification may also partially be the result of surface emissivity differences between the 3.7 and 10.8 micrometer parts of the spectrum. There were only a few very cold (TGCT) CLOUDY arrays (with  $T_4$  around 240K), which would indicate rather thick high clouds. There were thin cirrus clouds identified by the CIRT, but these were not very spatially extensive (mostly MIXED category), and were rather warm ( $T_4 \sim 281K$ ). Fig. 5a shows that these thin cirrus clouds are associated with temperatures lower than the surrounding surface area, which according to Luo, et al, 1995, had a brightness temperature of 284.3K.

The nighttime, mostly-ocean Scene "G" is seen in Figure 5c to be classified by CLAVR-1 about equally into each of the three coverage categories. Fig. 5b shows that of the CLOUDY cases, low stratus clouds (ULST) predominate overwhelmingly (99%), the remaining 1% being colder (TGCT). The CLEAR pixels over the ocean were chiefly in a narrow range

of Ch-4 temperature around 282K, whereas over the coastal land area, the associated  $T_4$  varied from 275K to 291K. The low stratus appeared to be in several layers or thickness regimes, ranging in  $T_4$  from 278.5K to near 283.5K, actually warmer than the immediate CLEAR ocean.

Qualitative evaluations of scenes in this area indicate that low stratus clouds are diagnosed effectively at night by the ULST, especially over the sea, even where the stratus-top temperatures are within a few degrees (higher or lower) of the sea surface temperature. Over land, colder clouds were detected by the FMFT. Our interpretation of these as always being thin cirrus is questionable, however. We have conducted studies that show that cloud cold enough to be detected by the TGCT, would also have been detected by the FMFT, implying that these clouds, if cirrus, are not very thin. It is as likely that they are mid-level water clouds, as pointed out by Luo et al. (1995). This evaluation indicates that, although rare in occurrence, when thin cirrus is indicated by the CIRT, it indeed appears to be thin. This is evidenced by the associated Ch 4 temperatures being much closer to the cloudfree Earth-surface temperature than is the case with clouds detected by FMFT. Many of the CIRT classifications were of the MIXED category, implying that the higher temperatures may also be indicative of cloud not filling the radiometers field-of-view (FOV).

### 5.1.3 Scenes in Other Areas

Several nighttime scenes in the NE Africa/Saudi Arabia (not shown, but including a portion of the Red Sea) region from February 9, 1990 were studied because their Ch 4 images suggest the presence of large bands or areas of cirrus with little or no other type of cloud present. It was determined that when cold enough to be classed as CLOUDY by the TGCT, either of the two thin cirrus tests (FMFT or CIRT) would also have detected this variably-thick cirrus. All clouds not detected by the TGCT were detected by either the FMFT or CIRT, supporting the foregoing image interpretation.

Several scenes in Eastern Siberia in February 1990 were examined in some detail with respect to the performance of the FMFT, ULST, and CIRT in polar areas at night. One important finding is that the threshold used in the restoral test (FMFR) to detect cloudfree surfaces colder than the TGCT threshold, is not optimum. It would perform better if the threshold was a few tenths of a degree higher. A similar adjustment to the CIRT

threshold, which calls some apparently cloudfree areas CLOUDY, appears needed. Finally, it was found that the lower cutoff temperature for application of the ULST over land is probably set too high, as this test appears to have detected low stratus clouds over land at Ch3 temperatures as low as 240K.



Figure 6a. Gray-scale cloud image of an orbital segment of AVHRR Ch 2 LAC reflectance data over an Antarctic coastline.

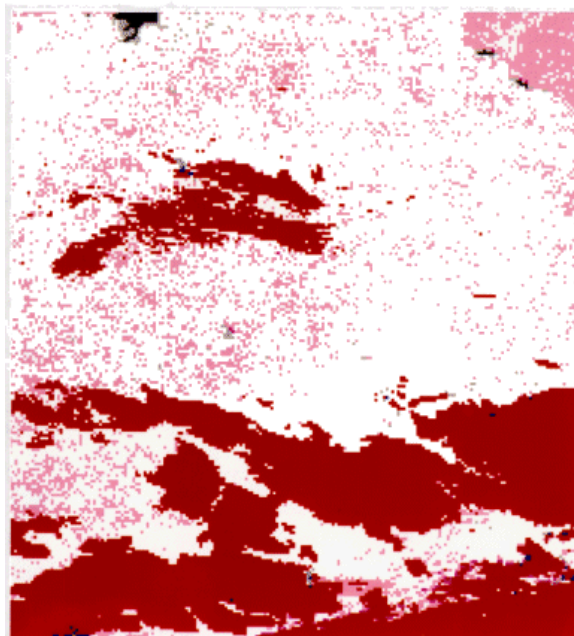


Figure 6b. Same segment shown in Fig. 6a, but showing color-coded classifications derived from the CLAVR-1 algorithm. Refer to Table 1 and Figures A1&2 to relate color to clear/cloud classification and algorithm path.

A number of daytime LAC (Local Area Coverage: pixel size 1.1km x 1.1km at nadir) scenes have also been studied. To illustrate the CLAVR-1 algorithm's ability to discriminate between snow/ice and cloud, one case from the Antarctic coast on December 23, 1986, is shown in Figure 6a (Ch 2 reflectance). With the predominance of sea ice and shelf ice in this image, and with the reflectance of this ice being comparable to that of clouds, it is difficult to distinguish the latter from the ice surfaces. Only some very dark areas, mostly just off the Antarctic ice shelves in the upper (southern) part of the image, are easily interpreted because they appear to be free of both ice and clouds. There are what appear to be clouds in the lower portion of the image. A considerably more definitive separation of ice from liquid water clouds is afforded by use of the Ch 3 albedo



restoral (C3AR) in the CLAVR-1 algorithm (see Figure 6b, a colorized image of the cloud classifications). Recall that ice or snow is not as reflective as water clouds in Ch 3, so restoral to CLEAR by the C3AR (white) serves well in distinguishing CLOUDY pixels (RGCT and FMFT) over snow or ice. However, thick ice-particle clouds in polar regions cannot be separated unambiguously from CLEAR ice or snow with the CLAVR-1 algorithm because the spectral signatures of the two surfaces are too similar.

## 5.2 Quantitative Evaluation of Cloud Amount

To assess the accuracy of cloud amount estimates made from CLAVR-1 classifications, a surface/cloud "truth" pixel analysis is provided using an image processor to display contrast-enhanced scenes derived from LAC or GAC data. Analysts interact with the imaged data by using the processor to independently estimate the amount of cloud in a fixed geographical area.

Historically, the detection and quantification of cloud cover from environmental satellite imagery has employed statistical analysis of the digital data rather than direct examination of the imagery (Coakley & Bretherton 1982; Rossow & Garder 1993). As part of the development of the CLAVR-1 algorithm, whose main thrust is an accurate delineation of CLEAR 2x2 GAC pixel arrays, a cloud "masking" capability was developed using contrast-signature threshold tests programmed into an image processor. The masks are exactly registered and superimposed upon a 100x100 pixel segment of an image from either of AVHRR Channels 1, 2, or 4. This system thus provides a means for visually masking the clouds interactively and computing that fraction of the segment interpreted to be covered by clouds by the analyst. Given a cloud amount output from the CLAVR-1 algorithm for this same segment enables a quantitative comparison of the two independent estimates of cloud cover amount. Although the analyst's cloud amounts cannot be expected to be perfect "truth", a previous study indicated that an analyst can estimate cloud amount with an accuracy of 0.05 - 0.10 in daytime and 0.10 - 0.15 at night (Stowe 1984).

The foregoing procedure for comparing computer and human estimates of cloud amount has been euphemistically dubbed "CLOUDBUSTER". The initial "CLAVR-1" algorithm when used to estimate cloud

amount assigns 50% cloud cover to all 2x2 pixel arrays classified as MIXED, and 0% and 100% for the CLEAR and CLOUDY arrays, respectively. This algorithm is termed the Fifty-Fifty Split (FFS) algorithm. The statistics reported here use intercomparison data sets from five GAC data scenes; three are daytime and two are nighttime. Although 20-25 (100x100 pixel) segments were defined for most scenes, one had only 12. The segments covered land, ocean, and coastal regions.

For all daytime segments, the following linear regression statistics (Stowe 1984) were computed (see Table 3): mean cloud amounts from CLOUDBUSTER and from the CLAVR-1 algorithm, along with their associated standard deviations; the root mean square error; the random error ( $\text{regression standard error}/2^{1/2}$ ); and the BIAS (difference of the means) of CLAVR-1 relative to CLOUDBUSTER. An overestimate by the CLAVR-1 algorithm would give a positive bias and an underestimate a negative one. Also calculated using the regression line slope and intercept was the projected bias if the CLOUDBUSTER cloud amount was 0% [ BIAS(0) ] and if it was 100% [ BIAS(100) ].

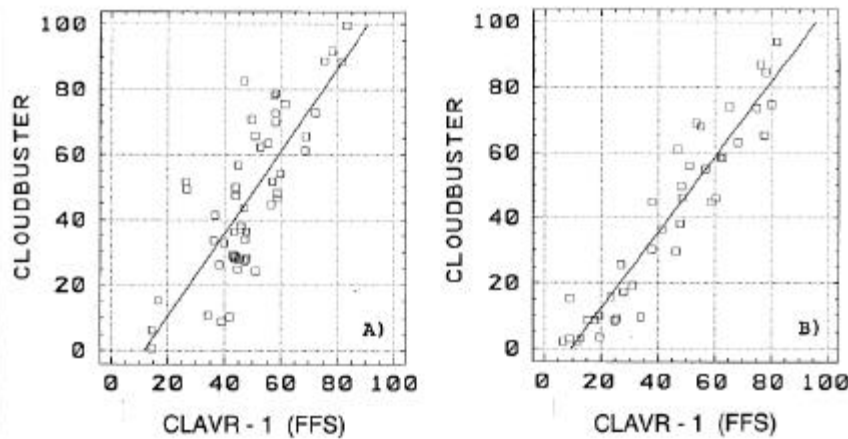


Figure 7. Regression relationship between CLOUDBUSTER (interactive computer estimate) and CLAVR-1 cloud amount (Fifty Fifty Split - FFS method) for 100 x 100 GAC pixel arrays from sample daytime and nighttime test images.

The BIAS (0) and BIAS (100) statistics in Table 3 demonstrate that the CLAVR-1 FFS cloud amount algorithm tends to overestimate the cloud amounts when CLOUDBUSTER says they are small and to underestimate when CLOUDBUSTER says they are large. Fig. 7 shows the CLAVR-1 mean values plotted against the CLOUDBUSTER cloud amounts for the two groupings of data discussed above. It illustrates the general tendency for the CLAVR-1 FFS algorithm to overestimate the cloud cover about 10% when it is small and to underestimate it by between 5 & 10% when it is large. This bias was also detected globally in a study comparing

different cloud algorithms, Hou, et al, 1993.

This is an expected consequence of MIXED (partly cloudy) pixel arrays tending to be less than 50% cloud covered when cloud amounts are small and greater than 50% when cloud amounts are large, as reported by Molnar and Coakley, 1985. They use this property of mixed pixels to derive a formula which effectively reduces this cloud amount bias in a statistical mean sense from regional (grid cell) estimates of cloud amount. We call this method the Statistically Equivalent Spatial Coherence (SESC) algorithm. It computes fractional amount of cloud within each grid cell as:

$$A_T = N_0/N_T + [0.5 + 0.5*(N_0/N_T - N_C/N_T)] * N_M/N_T$$

where  $A_T$  is total cloud amount; and  $N_C$ ,  $N_M$  and  $N_0$  are the populations of pixels with CLEAR, MIXED, and

CLOUDY classifications.  $N_T$  is total pixel count. As is evident from the equation, the SESC algorithm decreases cloud cover relative to the FFS method when the proportion of CLEAR pixels exceeds the proportion of CLOUDY pixels (term in parenthesis is negative), and increases it when the proportion of CLOUDY pixels exceed the CLEAR pixels. To quantify this improvement over FFS, linear regression coefficients relating the FFS estimate to SESC for both ascending (daytime) and descending (nighttime) daily global data have been computed for one day. These have been substituted into the regression equation relating CLOUDBUSTER to FFS to estimate the slope and intercept relating CLOUDBUSTER to SESC. This exercise yields a BIAS(0) of +2.6% and a BIAS (100) of +0.6% for daytime; and a BIAS(0) of +0.1% and a BIAS(100) of +4.2% for nighttime for the SESC result relative to CLOUDBUSTER. Thus the SESC cloud amounts are less biased than the FFS values (see Table 3).

An independent assessment of the cloud amount biases in the FFS and SESC methods has been performed by Luo, et al, 1998 (submitted to this journal) compares these two cloud amount estimates with a more sophisticated interactive computerized image analysis for 36 one-degree lat/lon cells in the FIRE-II study area covering parts of Kansas and Oklahoma on the afternoon of November 28, 1991. Using the same statistical methods as in Table 3, these regression results give a FFS BIAS (0%) of 26.1% and a BIAS (100%) of -25%, whereas the SESC BIAS(0%) is 20.8% and the BIAS (100%) is -12%. Although these results are only for one day in a relatively small geographical areas and tend to be larger than when compared with CLOUDBUSTER, they still show that the SESC method gives cloud amounts in better agreement with interactive image analysis techniques than FFS.

In summary, putting more emphasis on the CLOUDBUSTER analysis of FFS coupled with the global relationship between FFS and SESC cloud amounts because of the greater range of conditions over which those statistics have been acquired, we conclude that the CLAVR-1/SESC cloud amount should be within about 5% - 10% of the values estimated by interactive image analysis, on average.

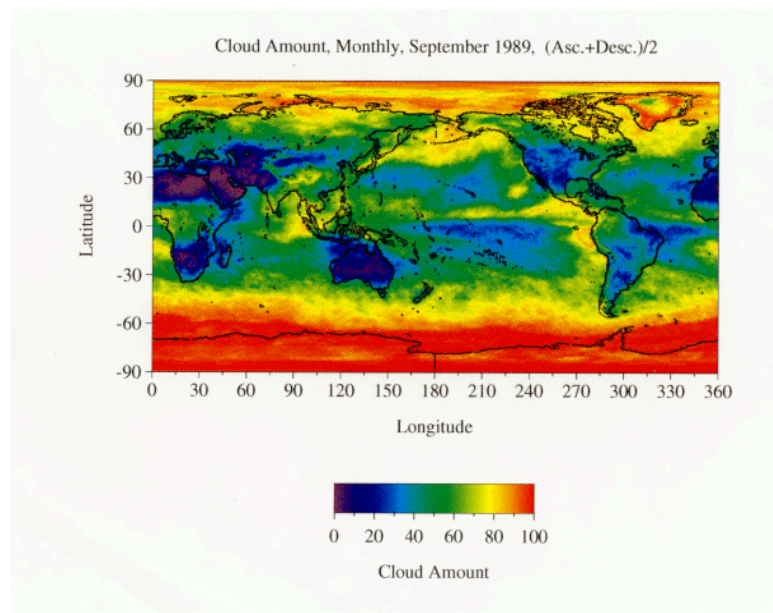


**Figure 8. Map of CLAVR-1 monthly mean total cloud amount (Statistically Equivalent Spatial Coherence - SESC method) for September, 1989, averaged for ascending (mostly daytime) and descending (mostly nighttime) orbital passes.**

To illustrate the characteristics of global cloud cover as derived by the CLAVR-1 SESC method, the monthly mean (ascending plus descending) cloud amount for September 1989 is shown in Figure 8. This date was chosen to be consistent with analyses presented in the companion CLAVR paper in this issue (Vemury, et al, 1998). The spatial distribution of cloud cover is consistent with two other global satellite climatologies: ISCCP, Rossow et al. (1993); and Nimbus-7, Stowe et al. (1989). In general, cloud cover is less than 30% over desert regions, 20-50% over sub-tropical anti-cyclonic circulation regions, and 50-80% in the mid-latitude storm tracks and the

intertropical convergence zone. CLAVR-1 has significantly more cloud cover than either of the other climatologies near the poles, with values between 80% and 100%. One known cause for CLAVR-1 to overestimate cloud cover in the poles results from the difference in snow/ice emissivity as a function of view angle between channels 4 and 5. The FMFT is used to restore cold pixels to clear in the nighttime algorithm, and because of these emissivity effects, fails to restore these cold pixels to clear when viewing snow or ice. The CLAVR-2 algorithm has removed this overestimate by implementing a FMFT threshold which is a function of view angle (Davis, et al, 1998).

## 6.0 DISCUSSION AND CONCLUDING REMARKS

The bases of cloud detection with multi-spectral imager data have been discussed, and their application to global AVHRR data by means of a cloud classification algorithm (viz. CLAVR-1) has been elaborated. Theoretical and empirical evidence has been presented to support the specifics of the algorithm. The algorithm has been evaluated by computer-enhanced image analysis of segments of orbital data, as well as by statistical

comparisons of derived total cloud amount with an analyst's interpretation of these images. Intercomparisons of total cloud amount at the mapped grid resolution with other global cloud data sets have been published elsewhere (Hou et al. 1993) and will be the subject of future publications.

Although the nighttime land algorithm works quite well during the summer, and in the subtropics and tropics at all seasons, its performance degrades at middle and high latitudes, particularly in the winter season and in mountainous terrain. The land surface, especially when snow covered, can become very cold at night, sometimes colder than the tops of the overlying clouds. In irregular terrain, especially in light winds, nocturnal temperature inversions are prevalent and surface temperature variability is often large. The algorithm for nighttime ocean scenes is simpler than the one for daytime scenes over land or ocean (e.g., only one restoral test is employed). Nevertheless, the nighttime algorithm appears to work rather well. Admittedly, its validation cannot be as reliable as that for the daytime algorithm because imagery is restricted to the three infrared channels.

Generally, the CLAVR-1 cloud amounts computed by assigning 50% cloud cover to MIXED pixel arrays (Fifty Fifty Split method) appear to be overestimated by about 10% when cloud amount is small and underestimated by about the same when cloud amount is large, when compared with an analyst's interpretation of visible and infrared images. Use of the Statistically Equivalent Spatial Coherence (SESC) method, where the fractional cover of mixed pixels is computed explicitly, reduces this bias to about 5% for the locations and dates studied. However, for certain geographical locations and seasons, larger errors have been observed. These result from: a) latitude/longitude boundaries affecting the cloud test sequence (see flow charts in Appendix); b) radiative similarities between cloud-free ocean sun-glint and low stratiform clouds; c) departure of land and snow/ice infrared emissivity from unity; and d) at latitudes greater than 50 degrees over ocean, some clouds are identified as sea-ice. These problems are being addressed in Davis, et al, 1998 and Vemury, et al., 1998.

Subsequent CLAVR algorithms (2 & 3) are nearing completion that should improve upon the quality of CLOUD/CLEAR classifications and will separate total cloud into amounts for different cloud types. New features include providing pixel-scale cloud classifications, gridded cloud amount by layered types (liquid phase, mixed phase, thick glaciated opaque, and semi-transparent ice), and maintaining the quality and increasing the

quantity of pixel-level CLEAR classifications, through the use of dynamic cloud/no-cloud threshold tests. These modifications also include a land surface type classification data base; snow/ice data bases; and an improved cloud test algorithm at polar latitudes.

Although not perfect, the results presented show that the CLAVR-1 classifications and cloud amounts are sufficiently accurate to justify testing their use in generating other climate parameters such as vegetation index, sea and Earth surface temperature and albedo, and atmospheric aerosol concentration over the oceans. The cloudy and cloud-free pixel radiances can be used to estimate Earth radiation budget, cloud and aerosol parameters and their radiative forcing. The initial effort to do this is the AVHRR Pathfinder Atmosphere (PATMOS) project (UCAR 1994). It uses cloud classified radiances and total cloud amount from CLAVR-1 to compute estimates of broad-band radiation budget parameters at the top of the atmosphere for all and clear-sky conditions, and aerosol optical thickness over the oceans. This is done on a daily, pentad and monthly basis, and on a 110 km equal-area global grid, for all NOAA afternoon satellites since NOAA/7, launched in 1981. This Pathfinder data set, currently sixteen years in extent, can be accessed electronically: <ftp://aries.nesdis.noaa.gov>. A paper is in preparation that evaluates the dataset quality and its usefulness for addressing climate-change questions.

## Acknowledgments

The authors are indebted to the following individual scientists and computer analysts who have used their skills and knowledge working on various parts of this project since its inception in 1988: P. Pellegrino, R. Carey, G. Gutman, C. Long, C. Duda, C. Watkins, and K. Campana, of NOAA; S. Hart, G. Major, D. Carr, C. Praderas, R. Yanamandra, L. Lu, B. Zhang, D. Moore, Y. Hou, S. Vemury, R. Anne, D. Love, G. Luo, F. Jing, of various contracting companies. We are also appreciative of the assistance given by management in NOAA, particularly G. Ohring, A. Gruber, H. Jacobowitz, and D. Tarpley of the Office of Research and Applications, and to W. Murray, of the NOAA/ Office of Global Programs. Funding for this work was provided by these two offices in support of new product development objectives in NESDIS and the NOAA Climate and Global Change Program objectives.

## APPENDIX. ALGORITHM DESCRIPTION

This Appendix presents flow charts to aid in understanding the CLAVR-1 algorithm described in Section 4.0. The theoretical basis for detection of thin cirrus and low stratus clouds with spectral signature tests is given. The spacecraft dependent coefficients for the Channel 3 albedo computation discussed in Sec. 3.1 are provided. Also, details of developing thresholds for the nighttime spectral signature tests (viz. the ULST, FMFT, and CIRT) which are functionally dependent upon the Ch 4 brightness temperature are presented. Finally, the equation for the GAMMA angle test used to treat specular reflection conditions is defined, as are some details of the RESTORED-CLEAR process.

### A1. Decision-Tree Flow Charts

Flow charts of the CLAVR-1 algorithm, as described in Section 3.4, are presented as Figures A1-A4. They show all paths that could be taken by a 2 pixel x 2 scanline array of AVHRR data. They also show the channel used, the name of the test, any special condition, and the cloud code used to represent the path taken. Square boxes represent threshold tests, diamonds represent special conditions for the tests, and hexagonal boxes represent the final classification categories. The numbers at the corners of the hexagonal boxes represent the cloud code which is unique to the path taken: upper left corner - CLOUDY; upper right corner - MIXED; lower left corner - CLOUDY AFTER BEING RESTORED TO CLEAR; lower right corner - MIXED AFTER BEING RESTORED TO CLEAR.

The algorithm is different when viewing land or ocean and when viewing by day or by night. CLAVR-1 uses a land/sea auxiliary data base with an equal-angle grid resolution of 1/16 degree (approximately 7 km at the equator) to specify what type surface is being viewed in a given pixel. If three or more of the pixels in an array are over land, the array is classified as land, otherwise it is classed as ocean or inland water surface. Certain tests are suspended over desert areas, which are approximated by rectangular latitude/longitude regions defined from Mathews (1985): Africa (land between 10N - 35N, 20W - 30E); Saudi Arabia - Western Asia (land between 5N - 50N, 30E - 60E); Central Asia (25N - 50N, 60E - 110E); and Australia (19S - 31S, 121E - 141E).



## A2. Cloud Radiative-Transfer Model

For three of the nighttime tests, one of which is also a daytime test (the FMFT), a simple cloud radiative-transfer model, adapted from Smith et al. (1974), is used to demonstrate how the brightness temperature differences between pairs of AVHRR channels vary with cloud optical thickness ( $\delta_c$ ) under several combinations of atmospheric and cloud conditions.

The cloud radiance model is as follows:

$$I = (\rho_s + N * (\rho_c - \rho_s)) * F + ((\tau_c - 1) * N + 1) * \epsilon_s * B_s + N * \epsilon_c * B_c \quad (A1)$$

Here  $N$  is the fractional cloud amount, and the model makes use of the conservation of energy principle requiring that the bulk reflectivity ( $\rho_c$ ), emissivity ( $\epsilon_c$ ), and transmissivity ( $\tau_c$ ) of a cloud sum to 1.0. Values of these optical properties for wavelengths approximately at the center of the three thermal channels of the AVHRR were taken from Hunt (1973) over a range of  $\delta_c$  for several modal cloud water droplet or ice particle radii ( $R_d$ ). Here we have used an optical thickness which is wavelength independent since, for a given  $\delta_c$ , the other optical properties of the cloud in Eqn A1 do allow for significant variations between 3.7, 10.8, and 11.9  $\mu\text{m}$ .

Restricting the study to cloud-filled pixels ( $N = 1.0$ ) over an ocean at night fixes the optical properties of the surface ( $\rho_s = 0.007$ ;  $\epsilon_s = 0.993$ ;  $\tau_s = 0$ ) and eliminates solar radiation ( $F = 0$ ). The temperature of the surface ( $T_s$ ) and the cloud ( $T_c$ ) are converted to Planck radiances ( $B_s$ ,  $B_c$ ).  $T_s$  is the cloudfree brightness temperature, which includes atmospheric attenuation unless "dry" is specified, in which case it is the physical surface temperature. Then, after supplying the optical properties corresponding to  $\delta_c$  values ranging from 0.01 (nearly transparent cloud) to 10.0 (virtually opaque cloud) or greater, for two water droplet sizes (5 and 10  $\mu\text{m}$ ) and three ice particle sizes (20, 40, and 100  $\mu\text{m}$ ), the model output consists of the Planck radiances ( $I$ ) corresponding to the central wavenumbers of Chs 3, 4 and 5. The final step is to convert these Planck radiances back to the corresponding Ch 3, Ch 4, and Ch 5 brightness temperatures ( $T_3$ ,  $T_4$ , &  $T_5$ ).

Figure A5 gives graphs of  $T_3$ - $T_5$  for a dry subtropical/mid-latitude atmosphere with  $T_s = 292\text{K}$ . Water

particles having  $R_d = 5 \mu\text{m}$  and  $10 \mu\text{m}$  are in Fig. A5a-A5c for  $T_c = 286\text{K}$ ,  $276\text{K}$ , and  $256\text{K}$ , respectively. The graphs clearly show how all the clouds are associated with substantially negative values of  $(T_3-T_5)$  when they are sufficiently opaque, particularly the lowest (warmest) clouds having small water droplets. This is the basis of the ULST test at night. Clouds with larger water droplets show the same effects as clouds with smaller droplets, but the variation with  $\delta_c$  is reduced. All but the warmest clouds also show a distinct positive peak in  $(T_3-T_5)$  for relatively thin clouds (at  $\delta_c = 1$ ). Thus, although the quantity  $(T_3-T_5)$  has been used chiefly for a ULST (opaque low clouds), it appears from these diagrams that it could also be useful for low/middle or middle clouds: the opaque ones having  $\delta_c > 10$  behave like low clouds, whereas the thin ones ( $\delta_c = 1.0$ ) behave like cirrus clouds. For comparison purposes an ice cloud at  $T_c = 236\text{K}$  with  $R_d = 20$  and  $40 \mu\text{m}$  is shown in Fig. A5d. As discussed in the text, this is the basis for the use of these two channels for cirrus detection at night.

Similar results are obtained for  $T_4 - T_5$ , but this has been well documented by others (Prabhakara et al, 1985, Inoue, 1986).

### A3. Calculation of the Ch 3 Albedo

The Ch3 Albedo Test (C3AT) first requires obtaining the Ch 3 albedo (C3A) using the following equations:

$$\text{C3A} = 3.14159 * \text{del}R_3 * 100\% / [\cos(Z_o) * (D_o/D)^2 * S_3] \quad (\text{A2a})$$

$$\text{del}R_3 = B(T_3) - B(T_{3e}) \quad (\text{A2b})$$

$$T_{3e} = b/a * T_4 - c/a * T_5 + d/a \quad (\text{A2c})$$

The variables in the above three equations are spacecraft dependent, and are given in Table A1 for the satellites where the CLAVR algorithm has been applied. In the above,  $\text{del}R_3$  is the estimated reflected radiance,  $S_3$  is the Ch 3 filtered solar irradiance at normal incidence and mean Earth/Sun distance,  $Z_o$  is solar zenith angle,  $(D_o/D)$  is the ratio of mean to actual Earth/Sun distance,  $B$  is the Planck function at the Ch 3 central wavenumber,  $\nu_o$ ,  $T_i$  is the observed equivalent black body (EBB) temperature in Ch(i), and  $T_{3e}$  is the estimated brightness temperature for Ch 3 due to emission only. The constants in Eqn (A2c) are derived from empirical relationships for cloudfree sea surface conditions that account for the attenuating effects of variable atmospheric-column water vapor

amounts (McClain et al. 1985).

#### A4. Establishment of Temperature-dependent Thresholds

The spectral-signature cloud tests, viz. the FMFT, ULST, and CIRT (see Sec. 3.2), use thresholds which are dependent on  $T_4$  to implicitly account for differences in water vapor absorption. They have been derived using 1200 globally-distributed cloudfree atmospheric soundings (905 for land and 295 for maritime stations) in a radiative-transfer model (Weinreb & Hill 1980) to generate a simulation data base of calculated  $T_3$ ,  $T_4$ , and  $T_5$  brightness temperatures, accounting for each channel's spectral response function. These thresholds have not been derived for each spacecraft, as it appeared from empirical studies that their application as cloud/no-cloud classifiers did not require that degree of precision. The total number of points is actually triple the above numbers because brightness temperatures were computed for three values of satellite zenith angle:  $sza = 0, 30$ , and  $60$  deg. These results were used to plot Figures 1-3 in Section 3.2.

$T_4$ -dependent Four-minus-Five (FMFT) ocean and land thresholds were defined by fitting fourth or fifth-degree polynomials in  $T_4$  to the maximum values of FMF for these cloudfree conditions. The simulation database was supplemented over land with some AVHRR data from daytime deserts to cover the observed dynamic range of the  $T_4$  measurements, including the effects of skin-shelter temperature discontinuities that are not in the simulation data base. The threshold has the following form:

$$\text{FMFT threshold} = \sum \{ a_i * T_4^i \} \quad i = 0 \text{ to } 4 \text{ or } 5 \quad (\text{A3a})$$

where Table A2 gives the sets of coefficients. The FMFT threshold equation for the ocean is applied when  $240\text{K} < T_4 < 287\text{K}$ . When  $T_4 < 240\text{K}$ , the threshold is set to zero. If  $T_4 > 295\text{K}$ , it is set to  $4.0\text{K}$ . When  $287\text{K} < T_4 < 295\text{K}$ , the following linear relation is used:

$$\text{FMFT threshold} = 0.154 * (T_4 - 287) + 2.77 \quad (\text{A3b})$$

For land surfaces, the FMFT threshold equation is applied in the  $T_4$  range from  $260\text{K}$  to  $305\text{K}$ . If  $T_4 < 260$

K, the threshold is set to zero; and if  $T_4 > 305\text{K}$ , it is set to  $7.8\text{K}$ , a number resulting from the inclusion of desert observations from AVHRR. When land surface temperatures become so high during daytime that Chs. 4 and/or 5 approach saturation values (viz., at and above about  $315\text{K}$ ), the FMFT is suspended.

The Uniform Low Stratus Test (ULST), based on the Ch3-Ch5 ( $T_3$ - $T_5$ ) temperature difference, is an important spectral signature test used in the MCSST nighttime algorithm to detect low stratus clouds (McClain et al., 1985). An exponential curve was fit to the middle of the sample of points to define the ULST threshold as follows:

$$\text{ULST threshold} = \text{EXP}(a + b * T_4) - 1.0 \quad (\text{A4})$$

where  $a = -9.375$ ,  $b = 0.0342$ ; the threshold varies from  $0.0$  to  $+1.4$  as  $T_4$  varies from  $273\text{K}$  to  $300\text{K}$ . Over land, the ULST is not applied if  $T_4 < 271\text{K}$  (lower limit of experience with ULST over oceans) or  $> 289\text{K}$  (maximum zonally-averaged, low-cloud temperature over land at night from Stowe, et al, 1989. In addition to this temperature restriction, it was found empirically that the constant  $(-1)$  used in Eqn (A4), needs to be lowered to  $-3.0$  to account for land surface emissivities less than unity at wavelengths near  $3.7 \mu\text{m}$  (Hovis, 1966).

The Cirrus Test (CIRT) is defined as  $(T_3 - T_5)/T_5$  and is shown in Figure 3. Although there are a few outliers present and the sampling is probably inadequate for the warmest and moistest air masses, one can reasonably define an upper limit, i.e. max CIRT, as a function of  $T_4$ . That upper limit has been chosen for the CIRT threshold, and is approximately represented for three ranges of temperature, as follows:

$$T_4 < 273\text{K}: \text{CIRT threshold} = 0.00$$

$$273 < T_4 < 292\text{K}: \text{CIRT threshold} = 1.77467 * (10^{-3}) * T_4 - 0.485328 \quad (\text{A5})$$

$$T_4 > 292\text{K}: \text{CIRT threshold} = 0.033$$

Problems can be encountered with tests involving Ch 3 (ocean or land) if electrical interference "noise", which has been present to a greater or lesser extent with this AVHRR channel on all the NOAA satellites to date, becomes too large (Warren 1989). Furthermore, it should be noted that Ch 3 brightness temperatures become

unreliable when they are lower than about 240K.

#### A5. GAMMA Equation (defining cone of specular reflection)

The restoral tests over ocean and Antarctica described in Section 3.4 are applied when viewing within a specified angular distance from the specular reflection direction for a plane ocean surface. The half-angle of this cone, GAMMA, is defined as:

$$\text{GAMMA} = \cos^{-1} [\cos(Z_o) * \cos(Z) + \sin(Z_o) * \sin(Z) * \cos(A)] \quad (\text{A6})$$

where  $Z_o$  and  $Z$  are solar and satellite zenith angles, respectively, and  $A$  is relative azimuth angle ( $A < 90$  deg viewing toward the specular ray,  $A > 90$  deg viewing away from it).

#### A6. Some Details of the Daytime RESTORED-CLEAR Process

With reference to Figs. A1 & A2, a threshold of 3% is chosen for the daytime Ch3 Albedo Restoral (C3AR) test; this is slightly above the reflectances of snow and sea ice reported in Warren (1984). All four pixels in the 2x2 array must be less than this threshold for the array to be classified RESTORED-CLEAR. Over oceans, the C3AR test is restricted to cold polar regions, as sea-ice tests are not necessary at other latitudes. Over land there is no such restriction, but the C3AR is skipped at latitudes poleward of 60S when viewing in a direction where specular reflection from Antarctic snow elevates this channel's reflectance above the threshold. This direction is determined by the GAMMA angle (see Sec. A5). In this case, GAMMA < 50 deg is used.

Pixels passing the daytime reflectance-based cloud tests over desert and other arid land types are subjected to a TGCT where the threshold is the temperature of the maximum zonally-averaged low-cloud temperature observed over sunlit land in the Nimbus-7 Cloud Climatology (viz. 293K---i.e., above the temperature of the warmest cloud observed by Nimbus-7 (Stowe et al. 1989)). Any MIXED or CLOUDY array where all four pixels have  $T_4$  greater than this threshold are classified RESTORED-CLEAR by this Thermal

Gross Cloud Restoral (TGCR) test. Because some non-desert land surfaces exhibit Ch 3 albedos greater than the 6% C3AT threshold, pixels passing this test are subjected to a Thermal Uniformity Restoral (TUR) test before the TGCR test is invoked. The TUR threshold is set empirically to 1.0K---using case studies it was found unlikely that a cloud would be this thermally uniform over daytime land areas.

Because of sunglint, a TUR test (in this case using a limit of  $< 0.5K$ ) is applied only when the satellite is viewing within the expected region of solar specular reflection defined by the GAMMA angle. Except for the very end of each satellite's lifetime, where it has drifted to late afternoon local observation times, a GAMMA angle of 40 degrees should define the angular space where most of this specular reflection ambiguity occurs. The Ch3 albedo is so sensitive to specular reflection, however, that the C3AT is bypassed when GAMMA less than 40 degrees (see Fig. A1). For the late afternoon orbits, specular reflection can be so intense when solar zenith angles exceed 45 degrees and GAMMA  $< 20$  deg, that the CLAVR-1 algorithm requires that all tests be bypassed (i.e., pixels treated as MISSING) in this geometrically-defined zone. This removes a high bias in cloud amount that results from CLEAR ocean pixels erroneously being called CLOUDY as the satellite progressively ages.

The specular reflection test assumes that clouds will have a stronger spatial signature than the cloudfree ocean in the infrared when viewing in the specular direction. However, some low stratus clouds can satisfy the thermal restoral test (viz. TUR), i.e., be thermally uniform to less than 0.5K. Thus, to avoid misclassification errors when processing the CLAVR-1 data sets, it has been learned to handle certain situations as follows: (1) treat RESTORED-CLEAR arrays passing the RGCT over ocean (cloud code identifies path) as CLOUDY (the RGCT threshold is much brighter than most specular reflection regions); and (2) treat pixels subjected to either of the next two reflectance tests in the daytime ocean sequence (RUT or RRCT), when restored to CLEAR, as MISSING. Even with the foregoing restrictions, it is still possible to classify pixel arrays as CLEAR in the region of specular reflection (see Vemury et al. 1998).

## REFERENCES

Ardanuy, P. E., L. L. Stowe, A. Gruber, and M. Weiss, 1989: Shortwave, longwave, and net cloud-radiative forcing as determined from Nimbus-7 observations. J. Geophys. Res., **96**, 18537-18549.

Baum, B. A., B. A. Wielicki, and P. Minnis, 1992: Cloud-property retrieval using merged HIRS and AVHRR data. J. App. Meteor., 31, 351-369.

Cess, R. D., C. G. Potter, J. P. Blanchet, G. J. Boer, S. J. Ghan, J. T. Kiehl, H. Le Treut, Z.-X. Li, X.-Z., Liang, J. F. B. Mitchell, J.-J. Morcrette, D. A. Randall, M. R. Riches, E. Roeckner, U. Schlese, A. Slingo, K. E. Taylor, W. M. Washington, R. T. Wetherald, and I. Yagai, 1989: Interpretation of cloud-climate feedback as produced by 14 atmospheric general circulation models. Science, 245, 513-516.

Coakley, J. A. and F. P. Bretherton, 1982: Cloud cover from high-resolution scanner data: detecting and allowing for partially filled fields of view. J. Geophys. Res., 87, 4917-4932.

Davis, P. D., G. Majors and H. Jacobowitz, 1984: An assessment of Nimbus-7 Earth Radiation Budget shortwave scanner data by correlative analysis with narrow-band CZCS data. J. Geophys. Res., 89, 5077-5088.

Davis, P.D., L.L. Stowe, G. Luo, and E.P. McClain, 1998: Automated Generation of Global Cloud Datasets from Polar Orbiting Satellites PartI: CLAVR-2 Orbital Pixel-Scale Multiple Layer Cloud Analyses (MLCA). To be submitted to JTECH.

Deirmendjian, D., 1969: Electromagnetic Scattering on Spherical Polydispersions. American Elsevier Publishing Co., Inc., New York, 290 pp

Dozier, J. And S. G. Warren, 1982: Effect of viewing angle on the infrared brightness temperature of snow. Water Resour. Res., 19, 5, 1424-1434.

Gutman, G., D. Tarpley, A. Ignatov, and S. Olson, 1995: The enhanced NOAA global land dataset from the Advanced Very High Resolution Radiometer. Bull. Amer. Met. Soc., 76, 1141-1156.

Hamill, T. M., R. P. d'Entremont and J. T. Bunting, 1992: A description of the Air Force Real-Time Nephanalysis Model. Weather Forecasting, 7, 288-306.

Hou, Y-T., K. A. Campana, K. E. Mitchell, S\_K. Yang, and L. L. Stowe, 1993: Comparison of an experimental NOAA AVHRR cloud dataset with other observed and forecast cloud datasets. J. Atmos. & Oceanic Tech., 10, 833-848.

Hovis Jr., W. A., 1966: Infrared spectral reflectance of some common minerals. Appl. Optics, 5, 245-248.

Hunt, G. E., 1973: Radiative properties of terrestrial clouds at visible and infrared thermal window wavelengths. Quart. J. Roy. Met. Soc., 99, 346-369.

Inoue, T., 1986: On the temperature and effective emissivity determination of semi-transparent clouds by bi-spectral measurements in the 10 micron window region. J. Met. Soc. Japan, 63(1), 88-99.

Kidwell, K. B., ed., 1991: NOAA Polar Orbiter Data User's Guide. NOAA National Environmental Satellite Data and Information Service, Washington DC 20233.

King, M. D., Y. J. Kaufman, W. P. Menzel, and D. Tanre, 1992: Remote sensing of cloud, aerosol, and water vapor properties from the Moderate Resolution Imaging Spectrometer (MODIS). IEEE Trans. Geos. and Rem. Sens., 30, 1, 2-15.

Luo, G., P. A. Davis, L.L. Stowe and E.P. McClain, 1995: A pixel-scale algorithm of cloud type, layer, and amount for AVHRR data. Part I: Nighttime. J. Atmos. & Oceanic Tech., 12, 1013 - 1037.

Luo, G., L.L. Stowe, P.D. Davis, 1998: An intercomparison of total and layered cloud amount between CLAVR and ISCCP for the November 28, 1991 FIRE-II region. Submitted to JTECH.

Mathews, E., 1985: Atlas of archived vegetation, land-use and seasonal albedo data sets. NASA Tech. Memo. 86199, Goddard Institute for Space Studies, New York, NY. 54 pages.



McClain, E. P., W. G. Pichel, and C. C. Walton, 1985: Comparative performance of AVHRR-based multichannel sea surface temperatures. J. Geophys. Res., 90, C6, 11,587-11,601.

McClain, E. P., 1989: Global sea surface temperatures and cloud clearing for aerosol optical depth estimates. Int. J. Rem. Sensing, 10, 763-769.

Mokhov, I. I., and M. E. Schlesinger, 1993: Analysis of global cloudiness. 1. Comparison of ISCCP, Meteor, and Nimbus 7 satellite data. J. Geophys. Res., 98, 12,849-12,868.

Mokhov, I. I., and M. E. Schlesinger, 1994: Analysis of global cloudiness. 2. Comparison of ground-based and satellite-based cloud climatologies. J. Geophys. Res., 99, 17,045-17,065.

Molnar, G. and J. A. Coakley, Jr., 1985: Retrieval of cloud cover from satellite imagery data: a statistical approach. J. Geophys. Res., 90, D7, 12,960 - 12,970.

Nakajima, T. And M. King, 1989: Determination of the optical thickness and effective particle radius of clouds from reflected solar radiation measurements. Part I: Theory. Jrnl. Atmos. Sciences, 47, 1878-1893.

Prabhakara, C., R. S. Fraser, G. Dalu, M. C. Wu, and R. J. Curran, 1988: Thin cirrus clouds: seasonal distribution over oceans deduced from Nimbus-4 IRIS. J. Appl. Met., 27, 379-399.

Rao, C. R. N. and J. Chen, 1994: Post-launch calibration of the visible and near infrared channels of the Advanced Very High Resolution Radiometer on NOAA-7, -9, and -11 spacecraft. NOAA Tech. Rep. NESDIS 78, Dept. of Commerce, Washington, DC, 22 pages

Rossow, W. B., and L. C. Garder, 1993: Cloud detection using satellite measurements of infrared and visible radiances for ISCCP. J. Climate, 6, 2341-2369.

Rossow, W. B., A. W. Walker, and L. C. Garder, 1993: Comparison of ISCCP and other cloud amounts. J. Climate, 6, 2394-2418.

Saunders, R. W., and K. T. Kriebel, 1988: An improved method for detecting clear sky and cloudy radiances from AVHRR data. Int. J. Remote Sens., 9, 123-150.

Schiffer, R. A., W. B. Rossow, 1983: The International Satellite Cloud Climatology Program (ISCCP): The First Project of the World Climate Research Program. Bull. Amer. Met. Soc., 76, 779-784.

Slingo, A., 1990: Sensitivity of Earth radiation budget to changes in low clouds. Nature, 343, 2653, 49-51.

Smith, W. L., 1974, H. M. Woolf, P. G. Abel, C. M. Hayden, M. Chalfant, N. Grody, 1974: Nimbus-5 Sounder Data Processing System Part I: Measurement characteristics and data reduction procedures. NOAA Tech. Memo. NESS 57, U. S. Dept of Commerce, Washington, DC, 99 pages.

Stowe, L. L., 1984: Evaluation of Nimbus-7 THIR/CLE and Air Force Three-Dimensional Nephanalysis estimates of cloud amount. Jrnl. Geophys. Res., 89, D4, 5370-5380.

Stowe, L. L., H. Y. M. Yeh, C. G. Wellemeyer, H. L. Kyle, & the Nimbus-7 Cloud Data Processing Team, 1989: Nimbus-7 Global Cloud Climatology, Part II: First year results. J. of Climate, 2, 671-709.

Stowe, L. L., E. P. McClain, R. Carey, P. Pellegrino, G. Gutman, P. Davis, C. Long, and S. Hart, 1991: Global distribution of cloud cover derived from NOAA/AVHRR operational satellite data. Adv. in Space Res., 11, 51-54.

Stowe, L. L., 1991: Cloud and aerosol products at NOAA/NESDIS. Palaeogeography, Palaeoclimatology, Palaeoecology (Global and Planetary Change Section), 90, 25-32.

Stowe, L. L., S. K. Vemury, and A. V. Rao, 1993: AVHRR Clear-sky Radiation Data Sets at NOAA/NESDIS. Adv. in Space Res., 14, 113-116.

Stowe, L. L., P. A. Davis, and E. P. McClain, 1995: Evaluating the CLAVR (Clouds from AVHRR) Phase I cloud cover experimental product. Adv. in Space Res., 16, 21-24.

Stowe, L.L., A.M. Ignatov, R.R. Singh, 1997: Development, validation and potential enhancements to the second generation operational aerosol product at NOAA/NESDIS. J. Geophys. Res., 102. D14, 16,923 - 16,934

Tarpley, J. D., S. R. Schneider, and R. L. Money, 1984: Global vegetation indices from the NOAA-7 meteorological satellite. J. Climate & Appl. Met., 23, 491-494.

UCAR, 1994: The NOAA-NASA Pathfinder Program, The University Corp. for Atmos. Research, Boulder, Colorado, 22 pages.

Uddstrom, M. J., W. R. Gray, 1996: Satellite cloud classification and rain-rate estimation using multi-spectral radiances and measures of spatial texture. Jrnl. App. Meteor., 35, 839-858.

Vemury, S., L.L. Stowe, R. Anne, 1998: AVHRR Pixel Level Cloud/No-Cloud Classifications Using Dynamic Thresholds (CLAVR-3). To be submitted to JTECH.

Warren, D., 1989: AVHRR channel-3 noise and methods for its removal. Int. J. Remote Sens., 4&5, 645-651.

Warren, S. G., 1984: Optical constants of ice from the ultraviolet to the microwave. Appl. Optics, 23, 1206-1225.

Warren, S.G., C. J. Hahn, J. London, R. M. Chervin, and R. L. Jenne, 1988: Global Distribution of Total cloud Cover and Cloud Type Amounts over the Ocean. U.S. Dept. of Energy, DOE/ER-0406, Washington, DC., 212 pages.

Weinreb. M. P., and M. L. Hill, 1980: Calculations of atmospheric radiances and brightness temperatures in infrared window channels of satellite radiometers. NOAA Tech. Rep. NESS 80, U. S. Dept. of Commerce,

Washington, D. C., 40pp.

Welch, R. M., S. K. Sengupta, and I. S. Kuo, 1988: Marine stratocumulus cloud fields off the coast of southern California observed using Landsat imager. Part II: Textural analysis. J. Appl. Meteor., 27, 363-378

Wielicki, B. A. and L. Parker, 1992: On the determination of cloud cover from satellite sensors: The effect of sensor spatial resolution. Jrnl. Geophys. Res., 97, 12,799 - 12,823.

Wylie, D. P., W. P. Menzel, H. M. Woolf, and K. I. Strabala, 1994: Four years of global cirrus cloud statistics using HIRS. J. Climate, 7, 1972-1986.

Yamanouchi, T. and S. Kawaguci, 1989: Cloud distribution in the Antarctic from AVHRR data of NOAA satellites and radiation measurements at the ground surface. IAMAP 89 Scientific Assembly, Reading, England, August, 1989.

## FIGURES

Fig. 1. Scattergram of Ch 4 minus Ch 5 (FMFT) brightness temperature difference versus Ch 4 brightness temperature computed from raobs using a radiative transfer model to simulate AVHRR data (cloudfree ocean and cloudfree land combined). CLAVR-1 FMFT-SEA threshold curve superimposed on data.

Fig. 2. Scattergram of Ch 3 minus Ch 5 (ULST) brightness temperature difference versus Ch 4 brightness temperature ( $T_4 > 271\text{K}$ ) computed from raobs using a radiative transfer model to simulate AVHRR data for a cloudfree ocean at night. CLAVR-1 ULST-SEA threshold curve superimposed on data.

Fig. 3. Same as Figure 1 & 2 except that  $(T_3 - T_5)/T_5$  (CIRT) is plotted versus  $T_4$ . CLAVR-1 CIRT threshold curve superimposed on data.

Fig. 4a. Gray-scale cloud image of an orbital segment of AVHRR Ch 2 GAC reflectance data over eastern tropical Africa in daytime. The location of two test scenes is shown.

Fig. 4b. Color-coded image of the same segment derived from the CLAVR-1 algorithm. Refer to Table 1 and Figures A1&2 to relate color to clear/cloud classification and algorithm path.

Fig. 4c. CLAVR-1 classification of the same segment into three categories of cloud cover: CLOUDY (white); MIXED (gray), and CLEAR (black).

Fig. 5a. Gray-scale cloud image of an orbital segment of AVHRR Ch 4 GAC temperature data over the southwestern USA in nighttime. The location of three test scenes is shown.

Fig. 5b. Same segment shown in Fig. 5a, but showing color-coded classifications derived from the CLAVR-1 algorithm. Refer to Table 2 and Figures A3&4 to relate color to clear/cloud classification and algorithm path.

Fig. 5c. CLAVR-1 classification of the same segment into three categories of cloud cover: CLOUDY (white);

MIXED (gray), and CLEAR (black).

Fig. 6a. Gray-scale cloud image of an orbital segment of AVHRR Ch 2 LAC reflectance data over an Antarctic coastline.

Fig. 6b. Same segment shown in Fig. 6a, but showing color-coded classifications derived from the CLAVR-1 algorithm. Refer to Table 1 and Figures A1&2 to relate color to clear/cloud classification and algorithm path.

Fig. 7. Regression relationship between CLOUDBUSTER (interactive computer estimate) and CLAVR-1 cloud amount (Fifty Fifty Split - FFS method) for 100 x 100 GAC pixel arrays from sample daytime and nighttime test images. These arrays were chosen from land, ocean and coastal regions.

Fig. 8. Map of CLAVR-1 monthly mean total cloud amount (Statistically Equivalent Spatial Coherence - SESC method) for September, 1989, averaged for ascending (mostly daytime) and descending (mostly nighttime) orbital passes. Resolution is one degree latitude and longitude.

#### FIGURES IN APPENDIX:

Fig. A1. Logical flow chart for daytime/ocean algorithm of CLAVR-1 code.

Fig. A2. Same as Figure A1 but for the daytime/land algorithm.

Fig. A3. Same as Figure A1 but for the nighttime/ocean algorithm.

Fig. A4. Same as Figure A1 but for the nighttime/land algorithm.

Fig. A5. Theoretical relationship of difference in brightness temperature between Chs 3 and 5 of AVHRR to cloud optical thickness,  $\delta_c$ , for different cloud particle radii,  $R_d$ , and cloud top temperatures,  $T_c$ : (a)  $T_c = 286K$ , (b)  $T_c = 276K$ , (c)  $T_c = 256K$ , (d)  $T_c = 236K$ . The radiative transfer computations (Eqn. A1) were done for a mid-latitude atmosphere without water vapor and at night with  $T_s = 292K$ . The droplets were assumed to be water in all but the last panel, where ice was assumed.

TABLES:

Table 1. Daytime cloud test thresholds.

Table 2. Nighttime cloud test thresholds.

Table 3. Statistics from CLOUDBUSTER intercomparisons.

TABLES IN APPENDIX

Table A1. Spacecraft dependent coefficients for Ch 3 albedo computation.

Table A2. Coefficients for FMFT threshold equations.

**TABLE 1: Daytime Cloud Test Thresholds**

	LAND SCENE					OCEAN SCENE			
<b>CLOUD/MIXED TESTS</b>	[Color]	Chan.	Thresh.	freq(%)		Chan.	Thresh.	freq(%)	
				<u>Cloud</u>	<u>Mixed</u>			<u>Cloud</u>	<u>Mixed</u>
RGCT (Refl Gross Cld Test)	[red]	1	>44% <sup>e</sup>	30.7	9.4	2	>30% <sup>e</sup>	30.6	13.7
RUT (Relf Unifrmty Test)	[dk.blue]	1	>9% <sup>e</sup>	na	7.4	2	>0.3% <sup>x</sup>	na	35.9
RRCT (Refl Ratio Cld Test)	[green]	2/1	0.9<R<1.1 <sup>x,e</sup>	1.7	1.6	2/1	0.9<R<1.1 <sup>x,e</sup>	t	t
C3AT (Ch 3 Albedo Test)	[yellow]	3,4,5	>6% <sup>e</sup>	1.4	1.7	3,4,5	>3% <sup>x</sup>	t	t
TUT (Thrml Unifrmty Test)	[lt.purple]	4	>3K <sup>e</sup>	na	13.3	4	>0.5K <sup>e</sup>	na	2.2
FMFT (Four - Five Test)	[pink]	4,5	>fcn T <sub>4</sub> <sup>th</sup>	16.4	3.7	4,5	>fcnT <sub>4</sub> <sup>th</sup>	4.7	1.4
TGCT (Thrml Gross Cld Test)	[lt.blue]	4	<249K <sup>e</sup>	t	0.0	4	<271K <sup>x</sup>	0.1	t
<b>CLEAR RESTORAL TESTS</b>									
C3AR (Ch 3 Albedo Restoral)		3	<3% <sup>x</sup>	na	na	3	<3% <sup>x</sup>	na	na
TUR (Thrml Unifrmty Restoral)		4	<1K <sup>e</sup>	na	na	4	<0.5K <sup>e</sup>	na	na
TGCR (Thrml Gross Cld Restoral)		4	>293K <sup>x</sup>	na	na	na	na	na	na
<b>CLEAR CLASSES:</b>									
PURE CLEAR	[black]				9.3				8.2
RGCT RESTORED	[white]				0.5				0.6
RUT RESTORED	[gray]				0.5				2.6
RRCT RESTORED	[gold]				0.9				t
C3AT RESTORED	[dk.purple]				1.5				0.0
	total freq(%) 100.0					100.0			

NOTES: "na" means not applicable ; "t" means trace, i.e 0.0<freq(%) <0.05; see Figs A1-A2 for RESTORED-CLEAR test channels and thresholds. Footnotes – Thresholds determined: “e” = empirically; “th” = theoretically; “x” = past experience.



**TABLE 2: Nighttime Cloud Test Thresholds**

	LAND SCENE					OCEAN SCENE			
<b>CLOUD /MIXED TESTS</b>	[Color]	Chan.	Thresh.	freq(%)		Chan.	Thresh.	freq(%)	
				<u>Cloud</u>	<u>Mixed</u>			<u>Cloud</u>	<u>Mixed</u>
TGCT (Thrml Grs Cld)	[red]	4	<249K <sup>e</sup>	42.2	6.3	4	<271K <sup>x</sup>	44.5	6.2
TUT (Thrml Unfnty)	[dk.blue]	4	>3K <sup>e</sup>	na	15.6	4	>0.5K <sup>e</sup>	na	33.1
(ULST (Unifm Low St)	[yellow]	3,5	<fcn T <sub>4</sub> <sup>th</sup>	0.5	0.3	3,5	<fcn T <sub>4</sub> <sup>th</sup>	5.7	1.5
FMFT (Four - Five)	[pink]	4,5	>fcn T <sub>4</sub> <sup>th</sup>	10.7	4.1	4,5	>fcn T <sub>4</sub> <sup>th</sup>	0.1	0.1
CIRT (Cirrus)	[lt.purple]	3,5	>fcn T <sub>4</sub> <sup>th</sup>	2.2	3.1	3,5	>fcn T <sub>4</sub> <sup>th</sup>	0.2	0.2
<b>CLEAR RESTORAL TESTS</b>									
FMFR(Four - Five Restoral)		4,5	<fcn T <sub>4</sub> <sup>th</sup>	na	na	4,5	<fcn T <sub>4</sub> <sup>th</sup>	na	na
<b>CLEAR CLASSES</b>									
PURE CLEAR	[black]				13.0				8.2
FMFR RESTORAL	[black]				2.0				0.2
	total freq(%) 100.0					100.0			

NOTES: "na" means not applicable; "t" means trace, i.e. freq(%) <0.05%; see Figs. A3-A4 for use of RESTORED-CLEAR tests in the sequence. Footnotes – Thresholds determined: “e” = empirically; “th” = theoretically; “x” = past experience.

**Table 3. Statistics from CLOUDBUSTER Intercomparisons**

	DAYTIME		NIGHTTIME	
	CLOUDBUSTER	CLAVR	CLOUDBUSTER	CLAVR
MEAN	47.1	49.1	39.2	43.3
STND. DEVIATION	23.9	14.4	27.6	22.6
SAMPLE SIZE	51.0		40.0	
RMS ERROR	15.5		10.5	
RANDOM ERROR	10.7		6.5	
CORRELATION COEFF. (%)	79.0		95.0	
BIAS(0)	11.8		9.4	
BIAS (MEAN)	2.0		4.1	
BIAS(100)	-9.1		-4.1	

**Table A1: Afternoon NOAA spacecraft-dependent constants used in Ch 3 Albedo computation**

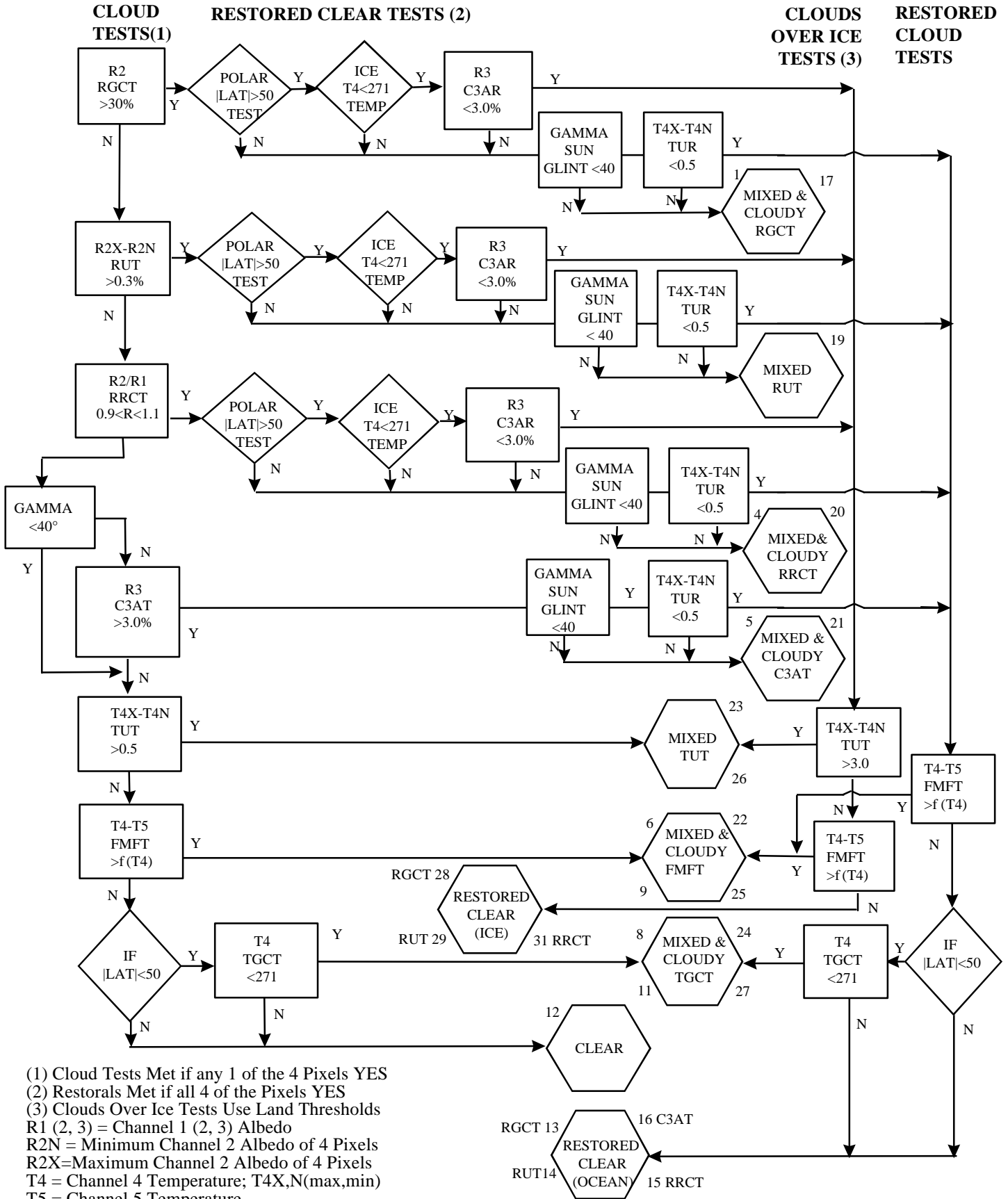
Spacecraft	$S_3$	$v_o$	$a$	$b$	$c$	$d$
NOAA-7	16.0872	2671.26	1.000000	-2.535500	1.56201	-6.71000
NOAA-9	16.1510	2677.68	0.982490	-2.659000	1.68550	-1.25000
NOAA-11	16.0707	2670.95	0.962422	-2.127582	1.16516	-0.74400
NOAA-14	15.8066	2645.90	1.000000	-2.915924	1.92754	-1.21284

**Table A2. FMFT threshold equation coefficients**

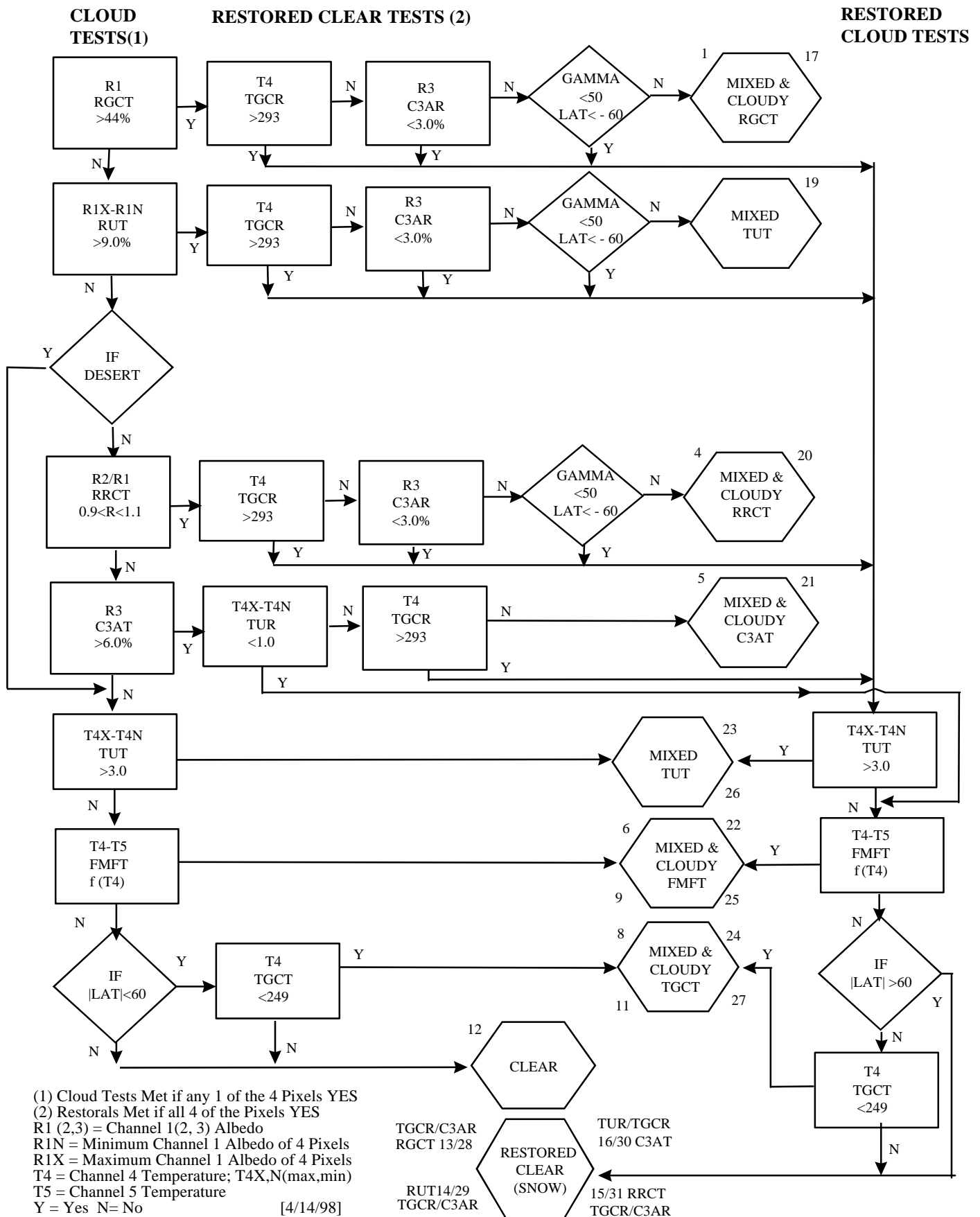
FMFT coefficients	FMFT-Ocean	FMFT-Land
$a_0$	9.27066E+04	-1.34436E+04
$a_1$	-1.79203E+03	1.94945E+02
$a_2$	1.38305E+01	-1.05635E+00
$a_3$	-5.32679E-02	2.53361E-03
$a_4$	1.02374E-04	-2.26786E-06
$a_5$	-7.85333E-08	0.0

# Figure A1: CLAVR-1 Decision Tree - Daytime Ocean

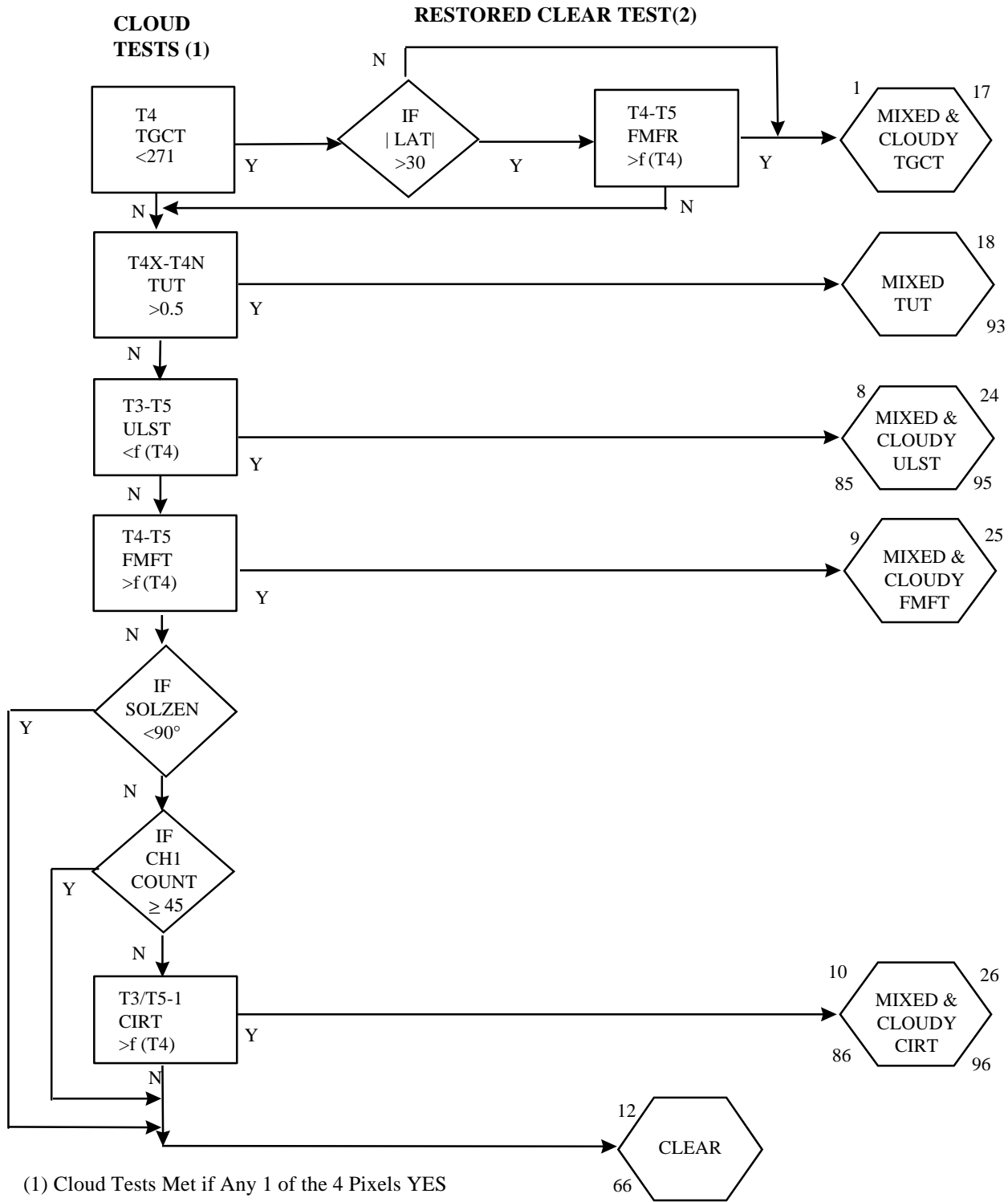
IF SOLAR ZENITH  $>45^\circ$  AND  $\gamma < 20^\circ$ , SKIP ALL OCEAN TESTS (CLASSIFY ARRAYS AS MISSING)



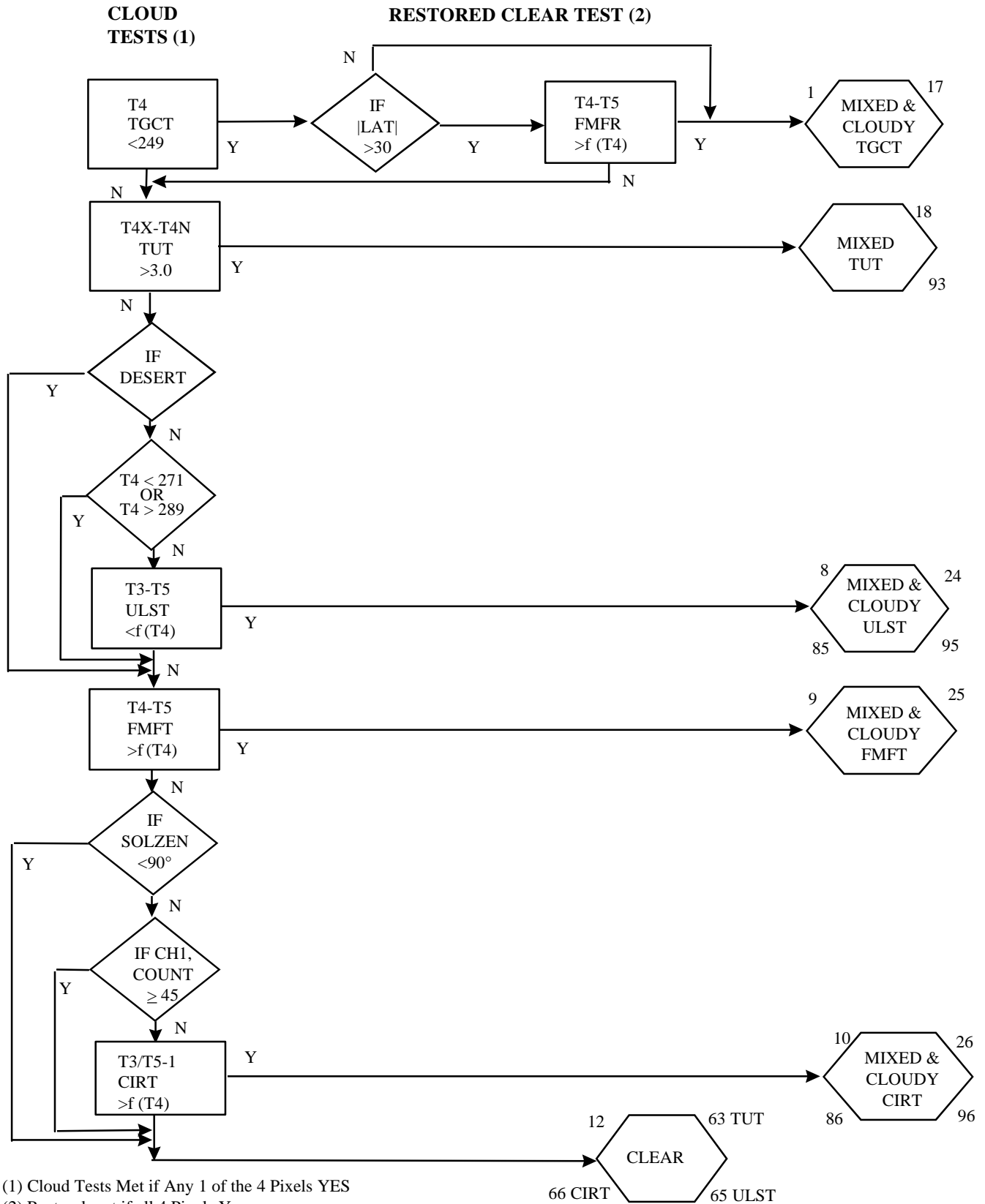
# Figure A2: CLAVR-1 Decision Tree - Daytime Land



**Figure A3: CLAVR-1 Decision Tree - Nighttime Ocean**



# Figure A4: CLAVR-1 Decision Tree - Nighttime Land



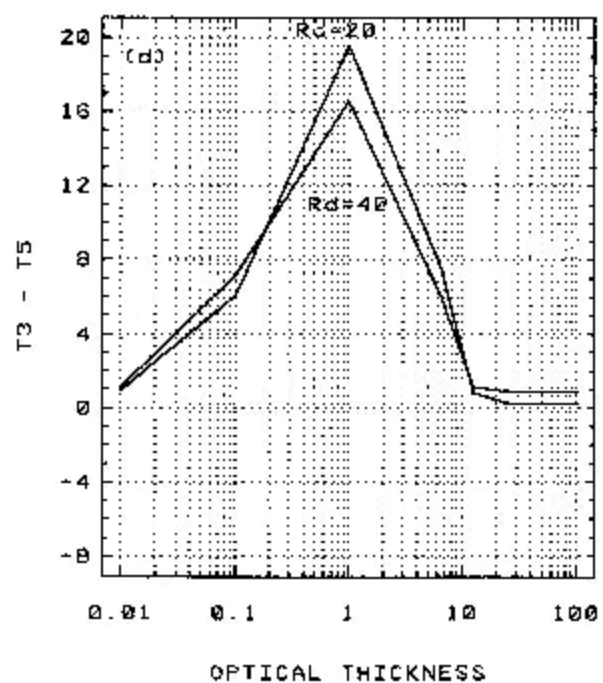
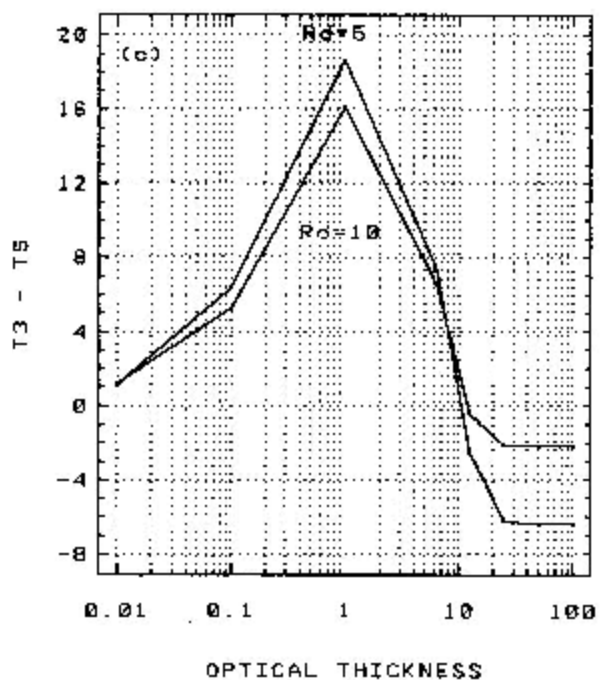
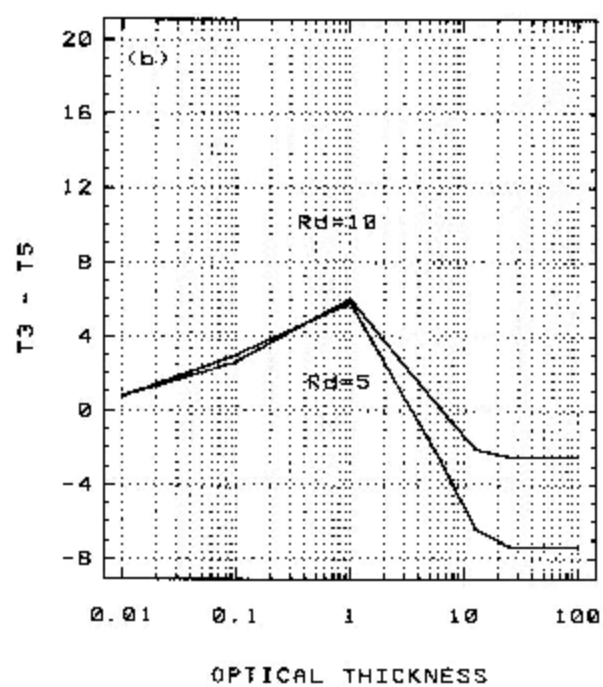
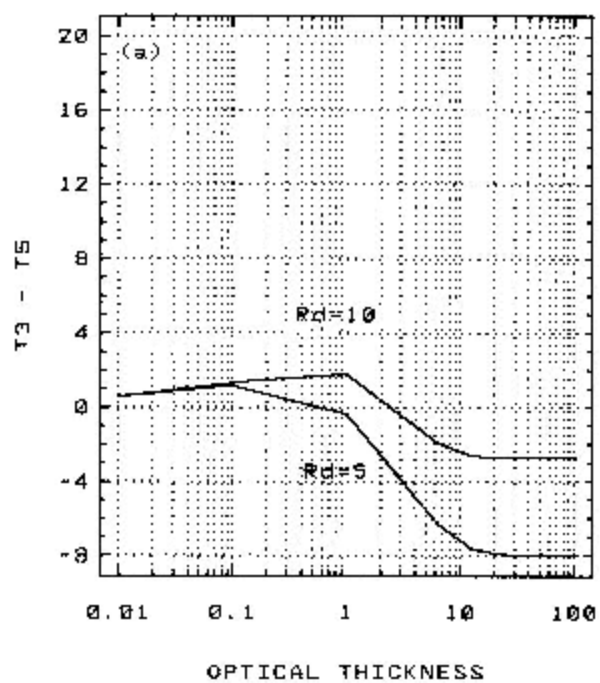


Figure A5

## FIGURES

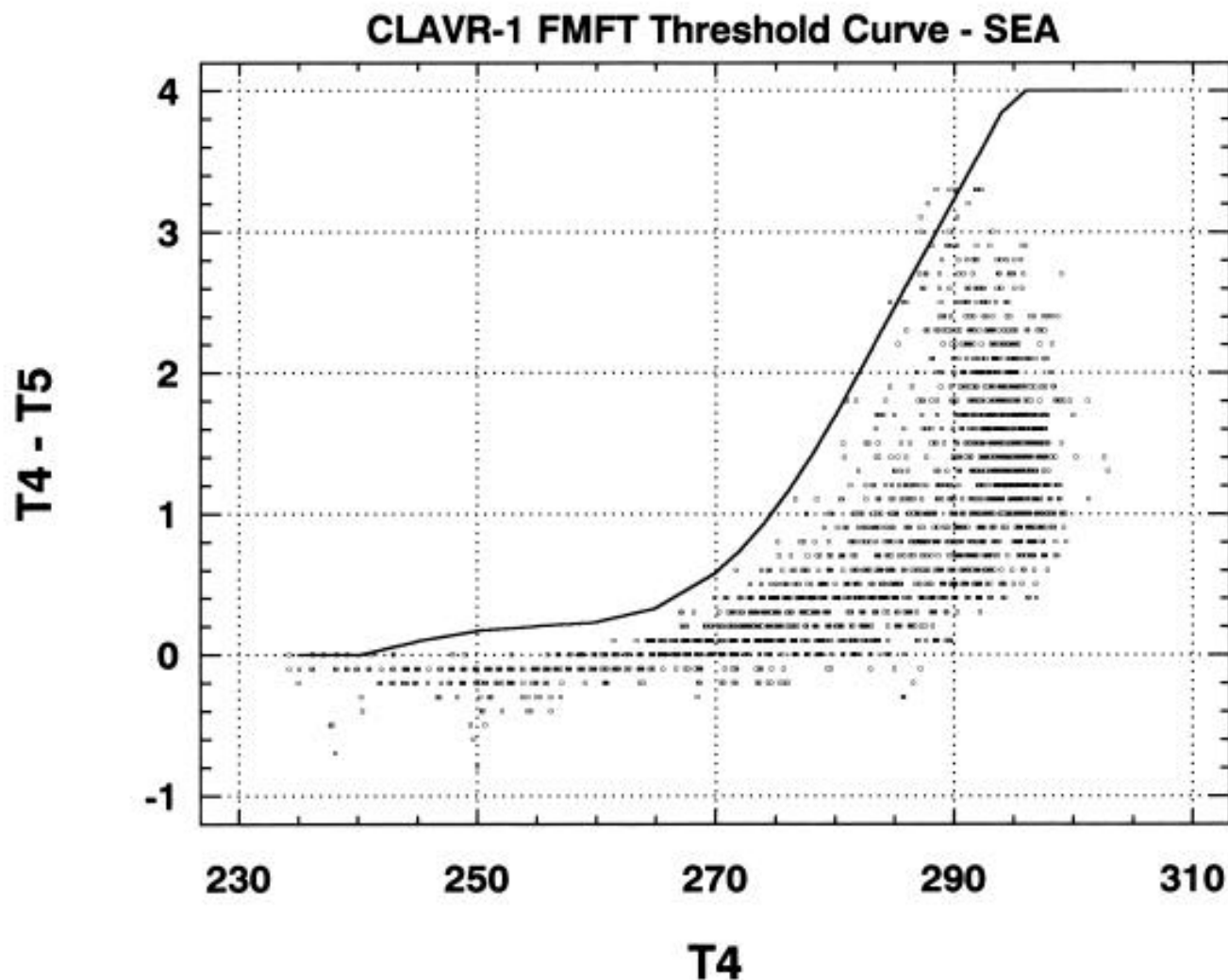


Fig. 1. Scattergram of Ch 4 minus Ch 5 (FMFT) brightness temperature difference versus Ch 4 brightness temperature computed from raobs using a radiative transfer model to simulate AVHRR data (cloudfree ocean and cloudfree land combined). CLAVR-1 FMFT-SEA threshold curve superimposed on data.



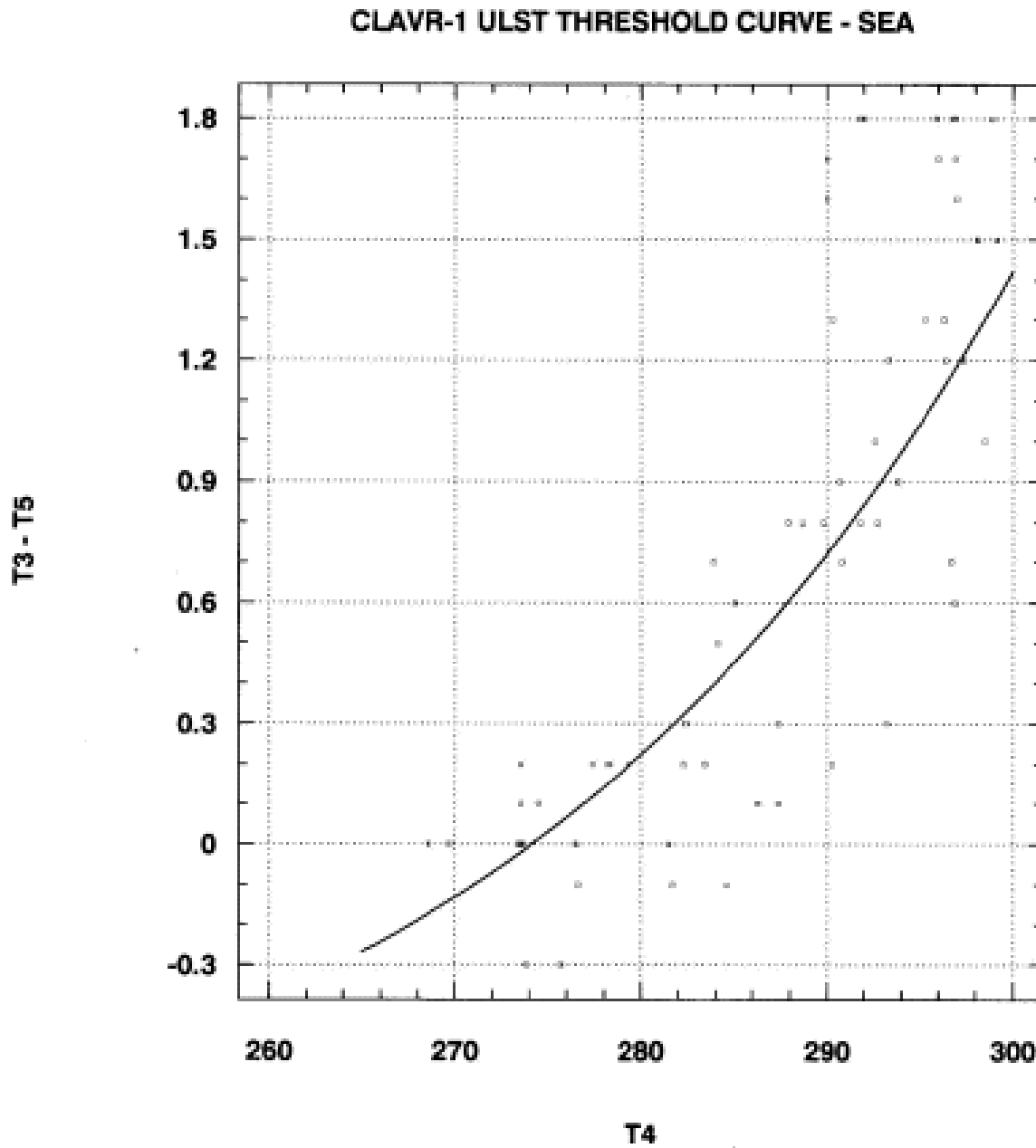


Fig. 2. Scattergram of Ch 3 minus Ch 5 (ULST) brightness temperature difference versus Ch 4 brightness temperature ( $T_4 > 271K$ ) computed from raobs using a radiative transfer model to simulate AVHRR data for a cloudfree ocean at night. CLAVR-1 ULST-SEA threshold curve superimposed on data.

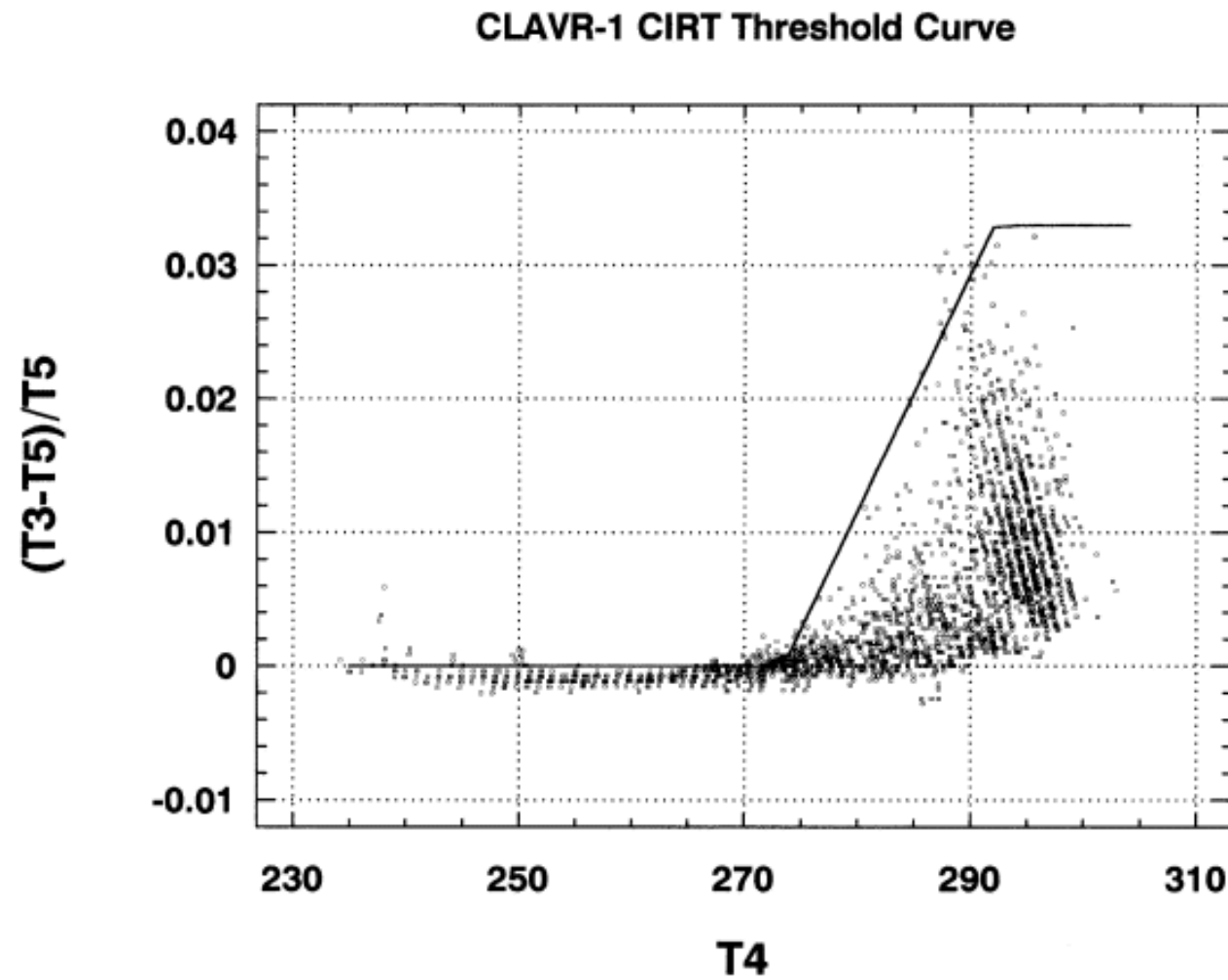


Fig. 3. Same as Figure 1 & 2 except that  $(T_3 - T_5)/T_5$  (CIRT) is plotted versus  $T_4$ . CLAVR-1 CIRT threshold curve superimposed on data.

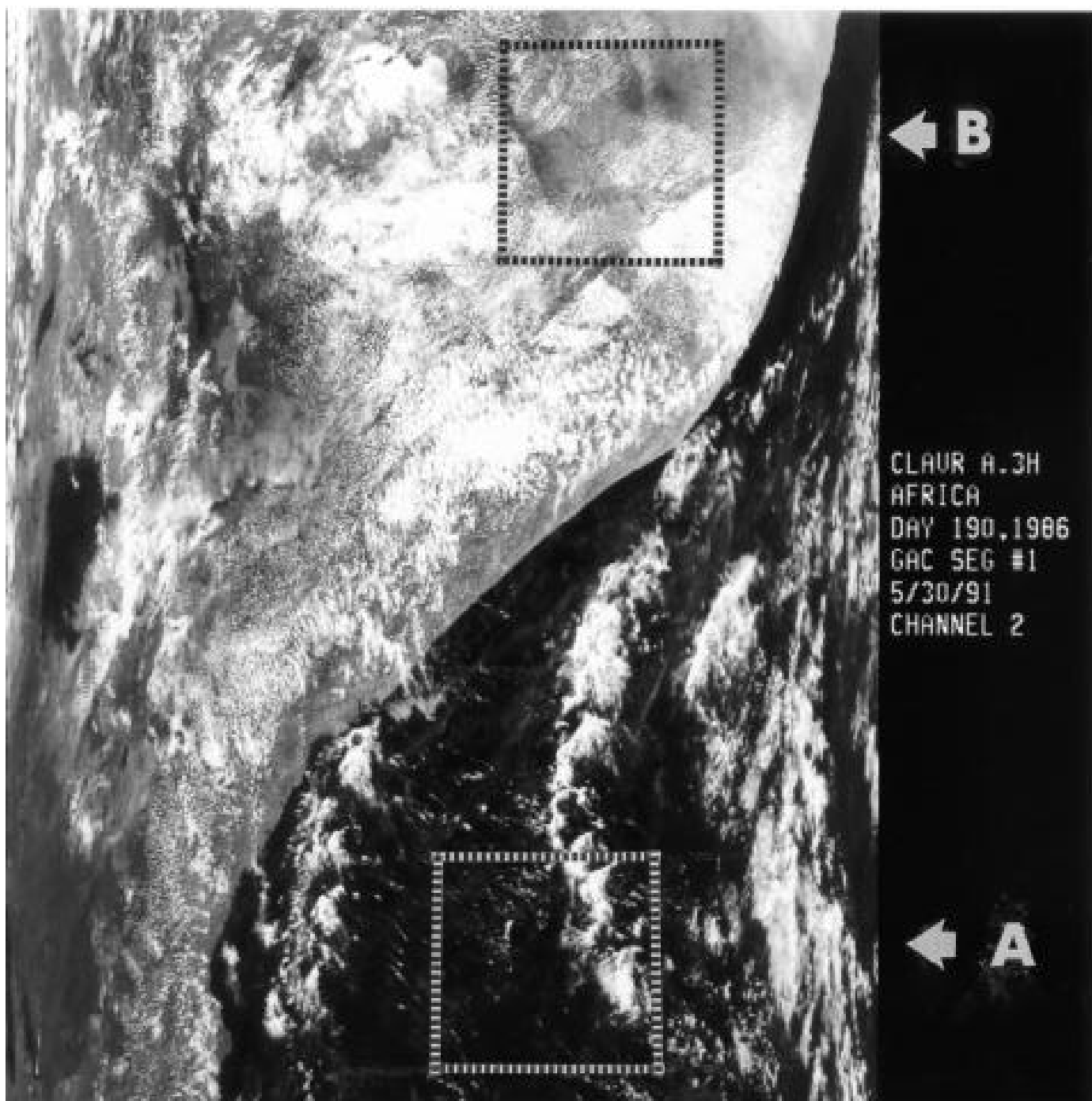


Fig. 4a. Gray-scale cloud image of an orbital segment of AVHRR Ch 2 GAC reflectance data over eastern tropical Africa in daytime. The location of two test scenes is shown.

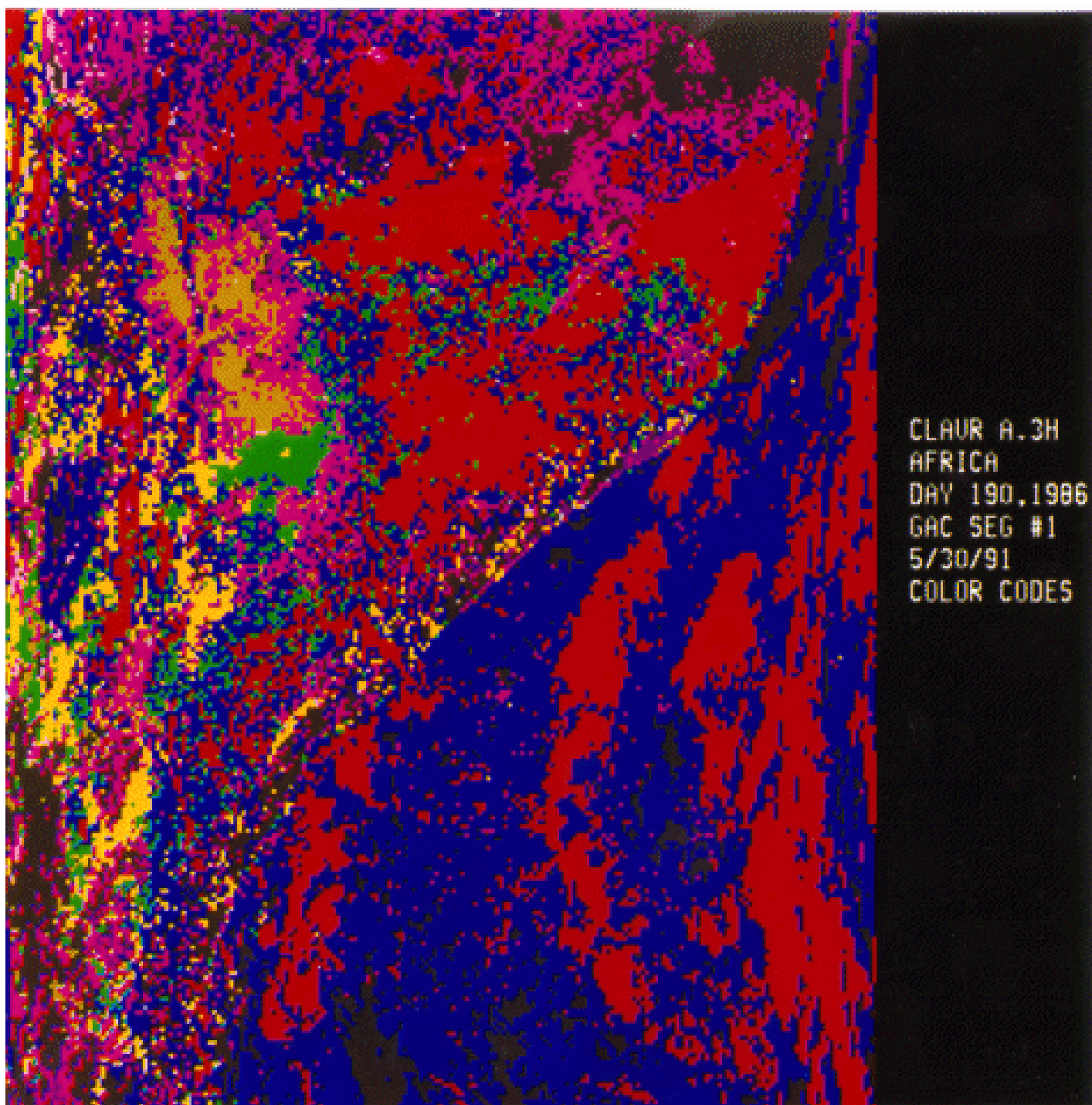


Fig. 4b. Color-coded image of the same segment derived from the CLAVR-1 algorithm. Refer to Table 1 and Figures A1&2 to relate color to clear/cloud classification and algorithm path.

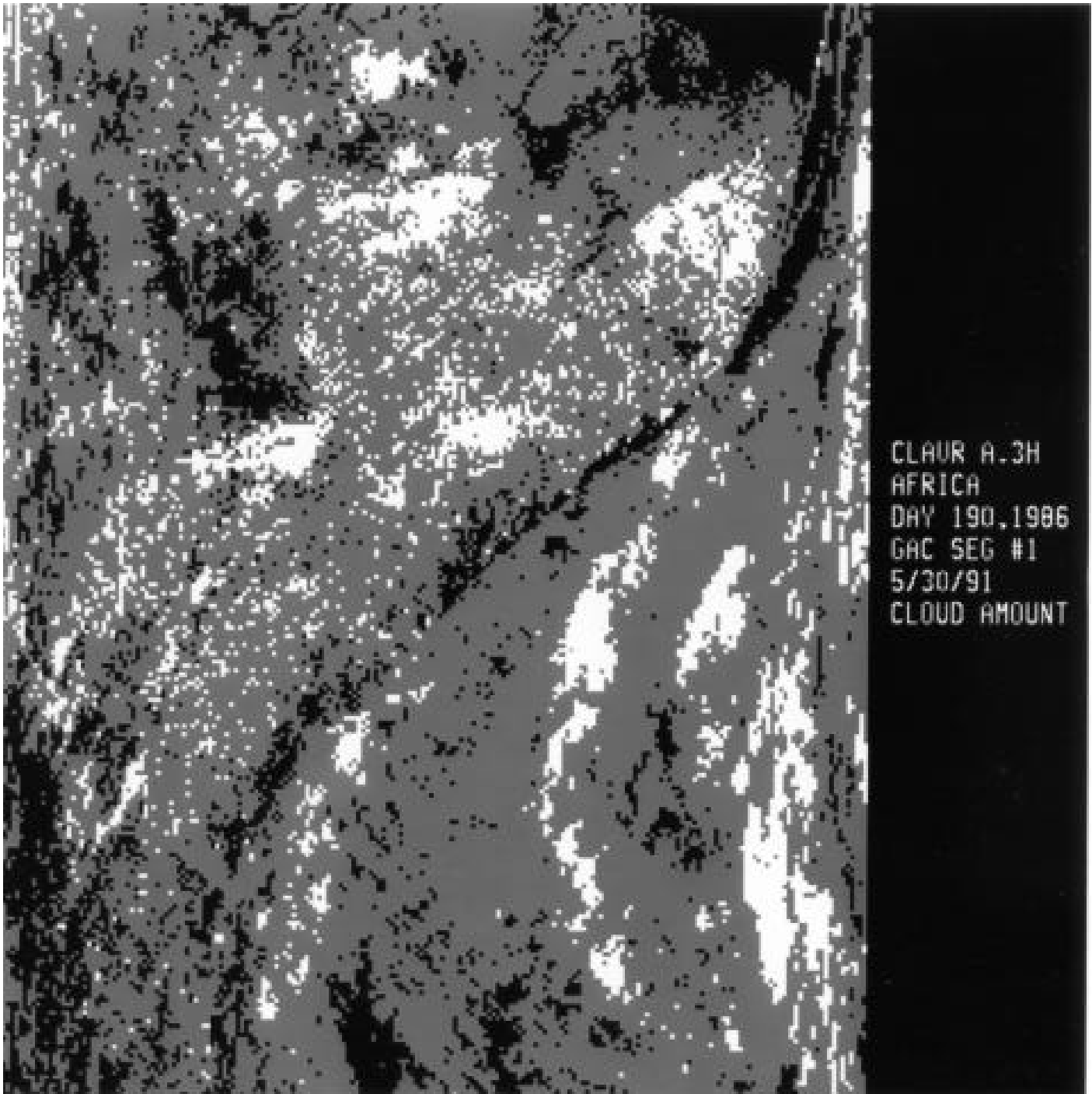


Fig. 4c. CLAVR-1 classification of the same segment into three categories of cloud cover: CLOUDY (white); MIXED (gray), and CLEAR (black).

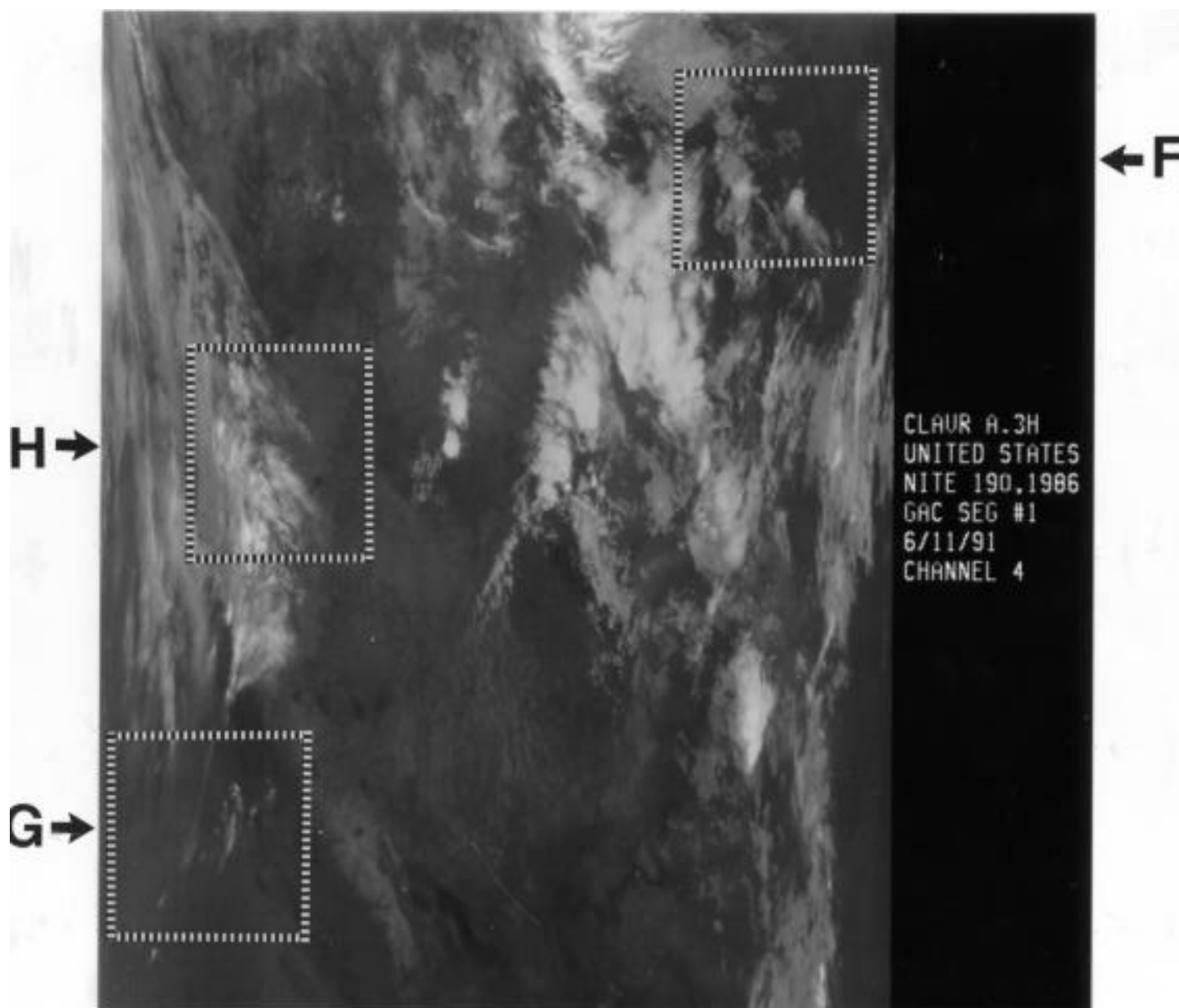


Fig. 5a. Gray-scale cloud image of an orbital segment of AVHRR Ch 4 GAC temperature data over the southwestern USA in nighttime. The location of three test scenes is shown.

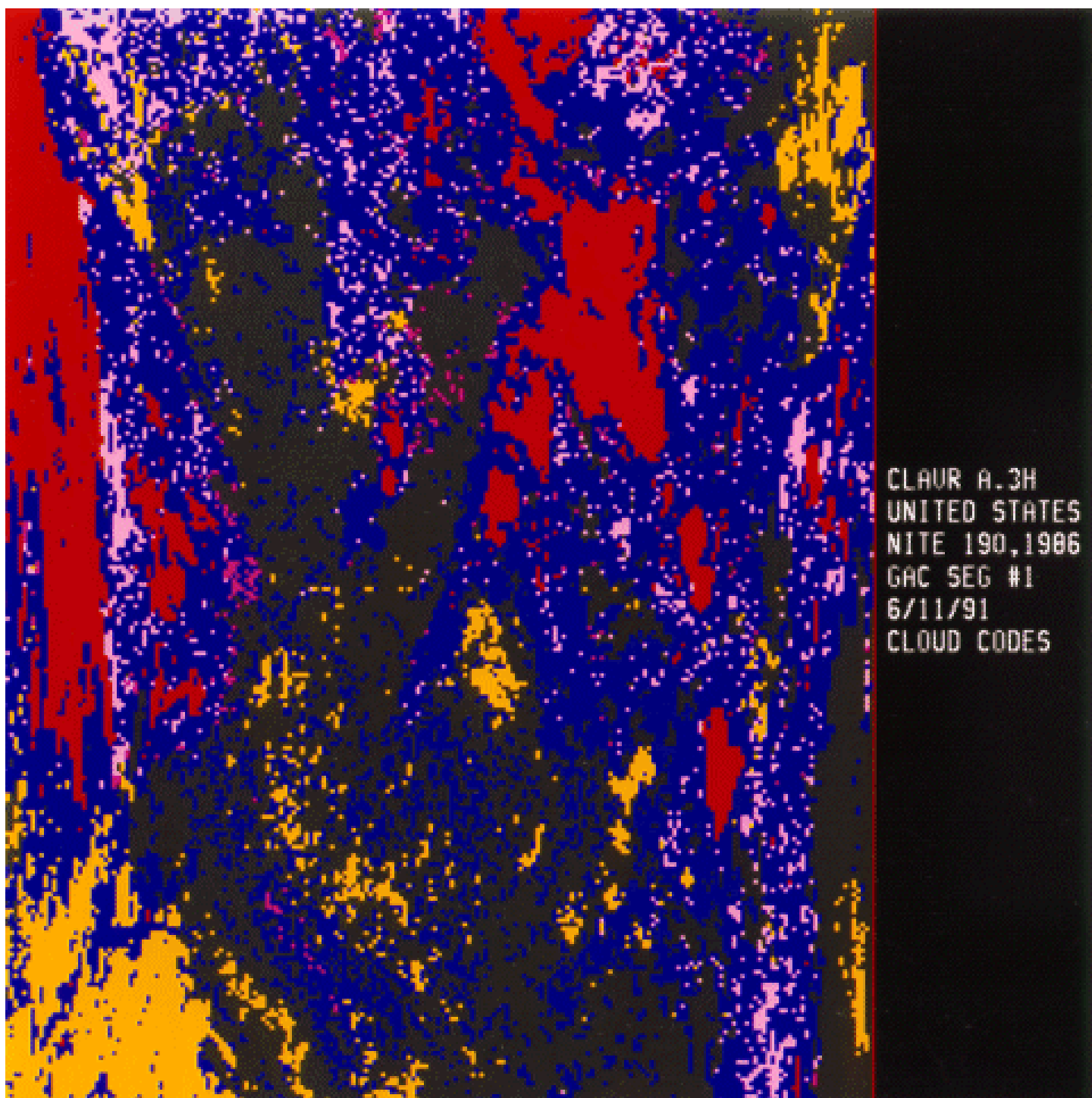


Fig. 5b. Same segment shown in Fig. 5a, but showing color-coded classifications derived from the CLAVR-1 algorithm. Refer to Table 2 and Figures A3&4 to relate color to clear/cloud classification and algorithm path.

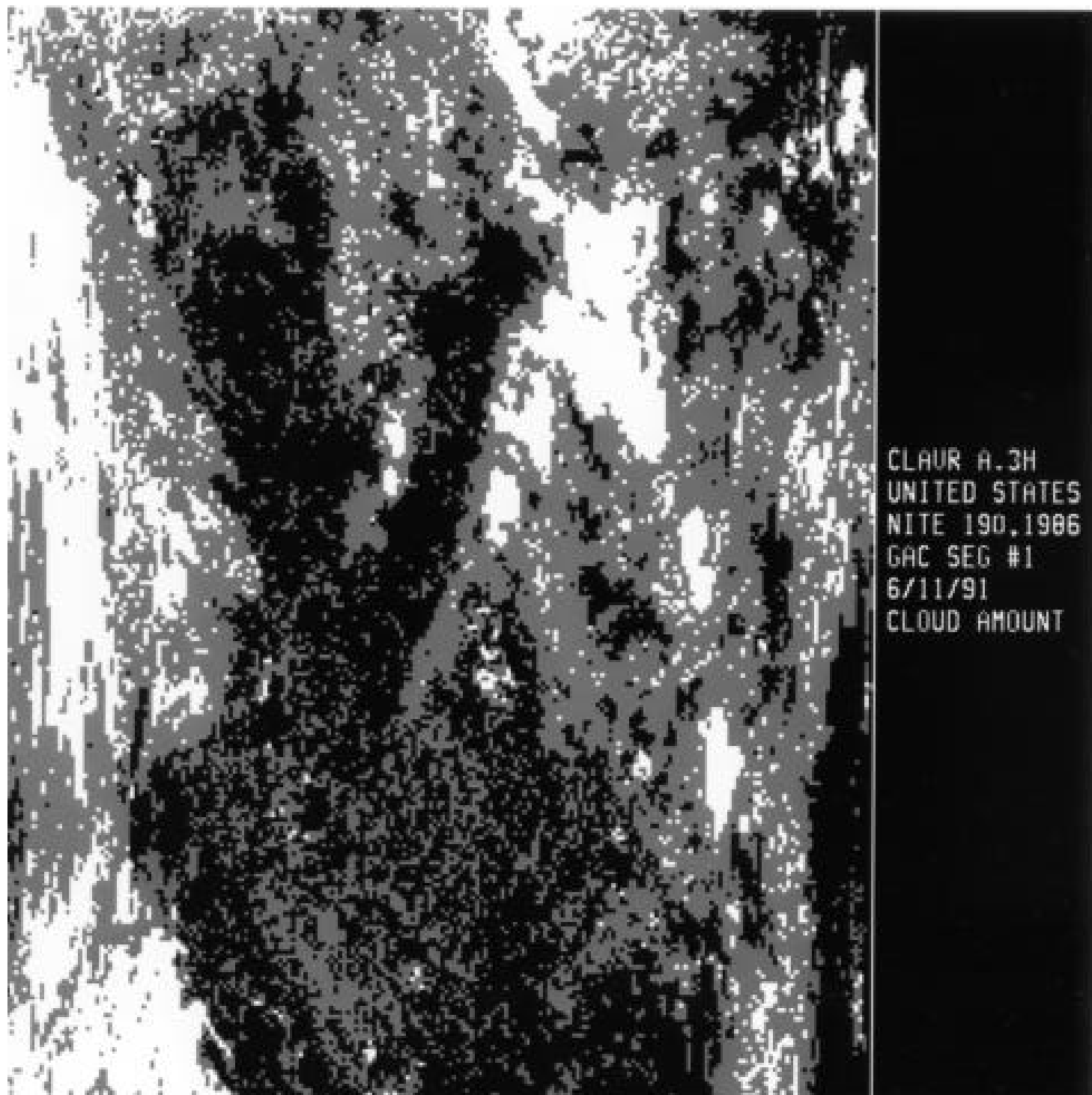


Fig. 5c. CLAVR-1 classification of the same segment into three categories of cloud cover: CLOUDY (white); MIXED (gray), and CLEAR (black).





Fig. 6a. Gray-scale cloud image of an orbital segment of AVHRR Ch 2 LAC reflectance data over an Antarctic coastline.

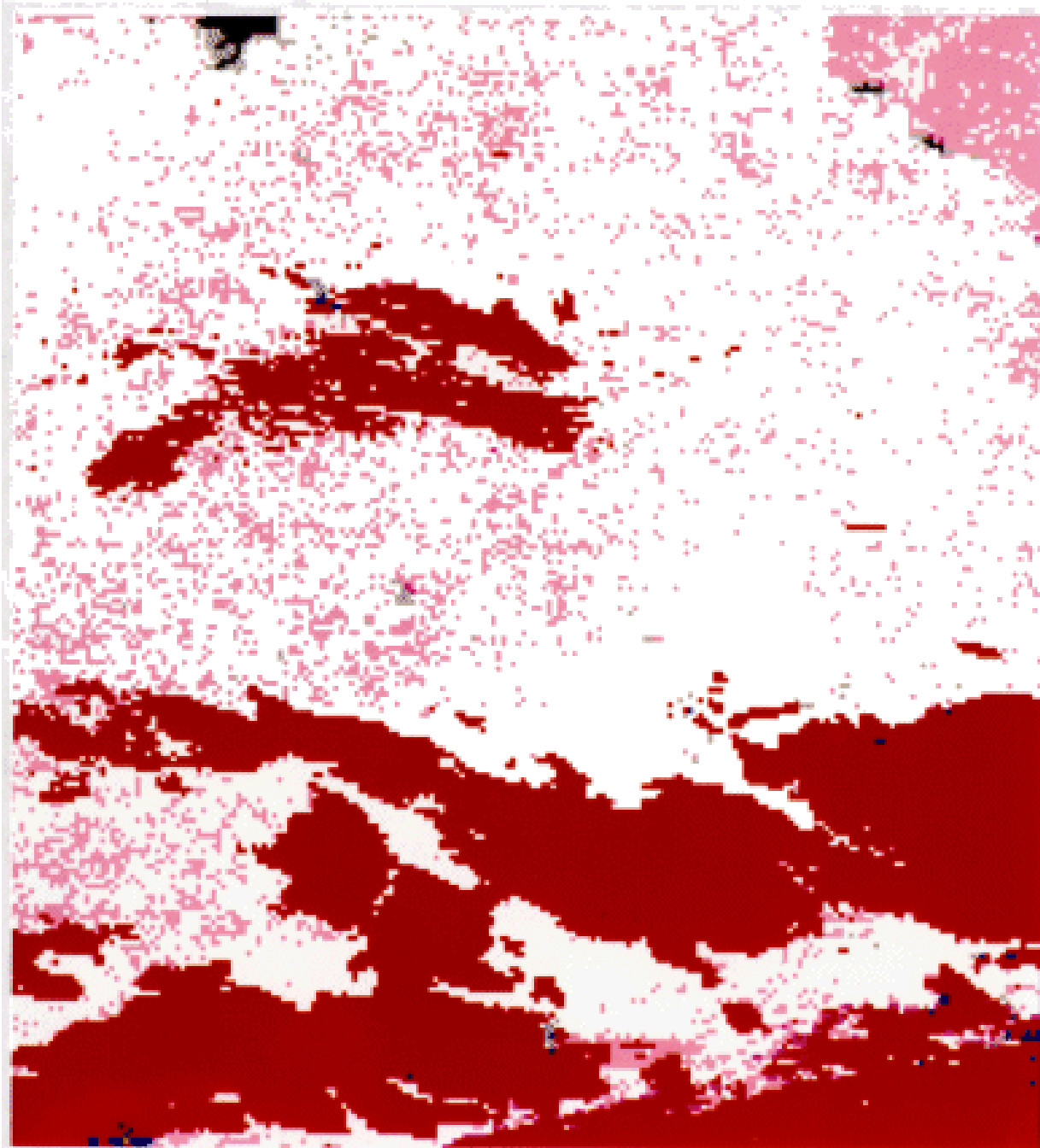


Fig. 6b. Same segment shown in Fig. 6a, but showing color-coded classifications derived from the CLAVR-1 algorithm. Refer to Table 1 and Figures A1&2 to relate color to clear/cloud classification and algorithm path.

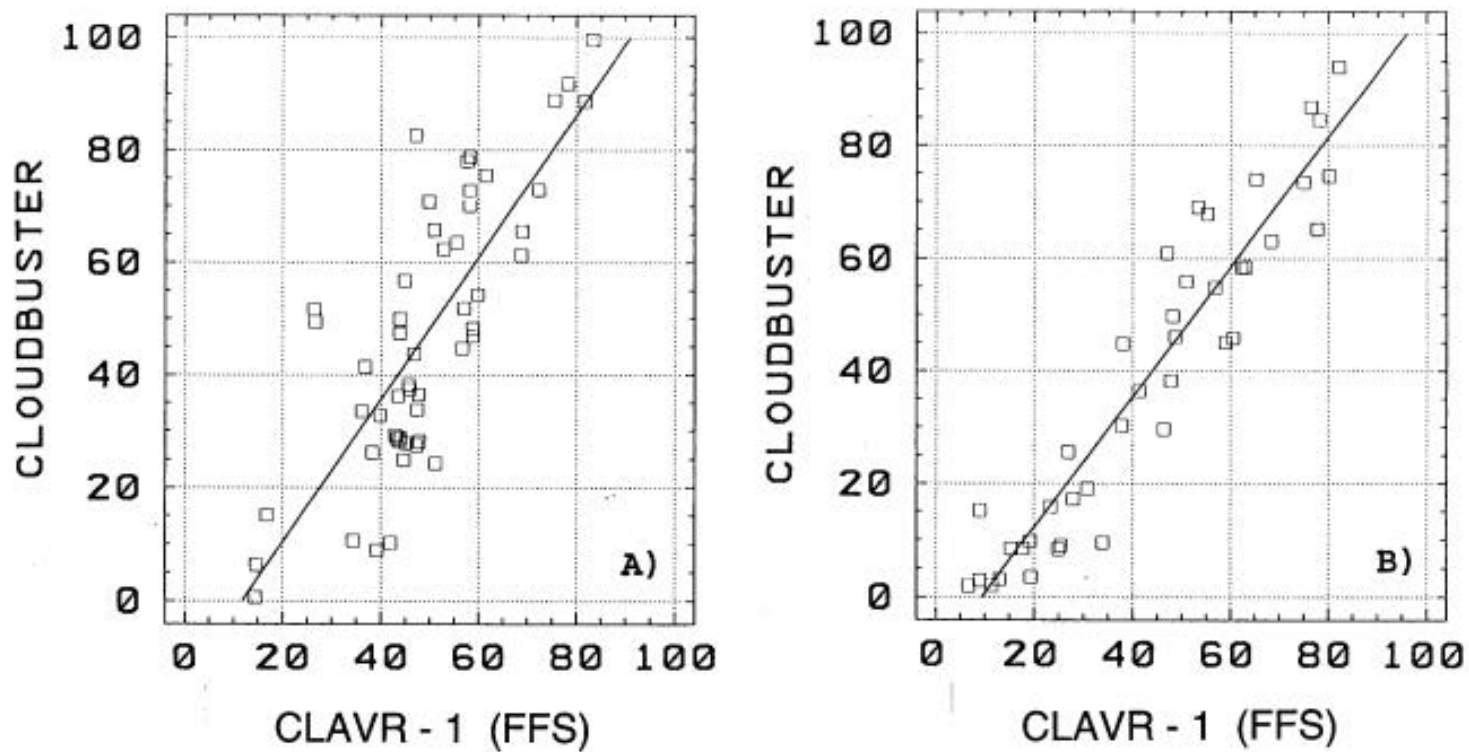


Figure 7

Fig. 7. Regression relationship between CLOUDBUSTER (interactive computer estimate) and CLAVR-1 cloud amount (Fifty Fifty Split - FFS method) for 100 x 100 GAC pixel arrays from sample daytime and nighttime test images. These arrays were chosen from land, ocean and coastal regions.

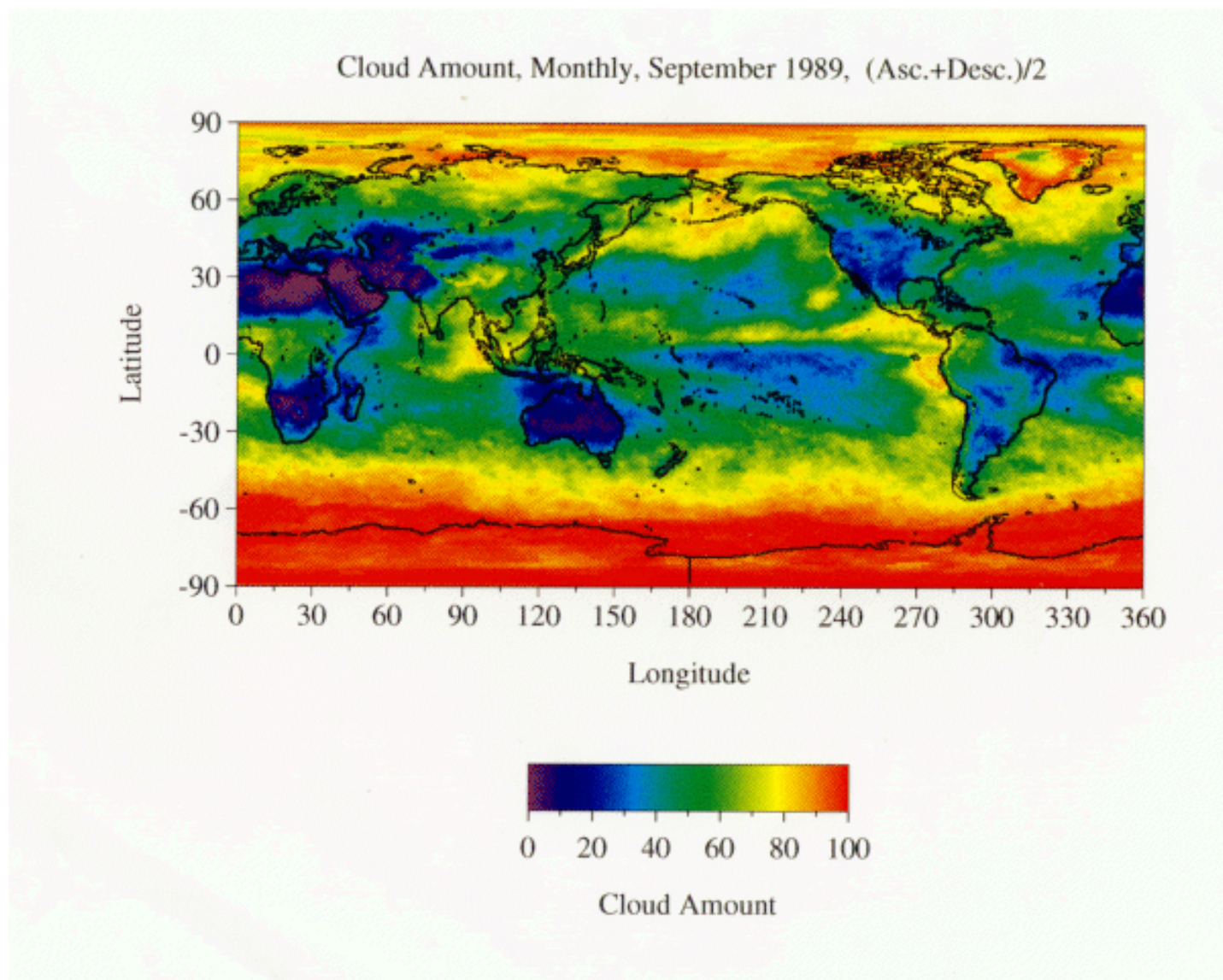


Fig. 8. Map of CLAVR-1 monthly mean total cloud amount (Statistically Equivalent Spatial Coherence - SESC method) for September, 1989, averaged for ascending (mostly daytime) and descending (mostly nighttime) orbital passes. Resolution is one degree latitude and longitude.